Journal of Building Engineering 93 (2024) 109801

Contents lists available at ScienceDirect

Journal of Building Engineering

journal homepage: www.elsevier.com/locate/jobe

Interface bonding characteristics of 3D printed ultra-high performance concrete after elevated temperatures

Liang Dong [a], Yekai Yang [c], Zhongxian Liu [a,**], Yan Zhang [a], Chengqing Wu [b,*]

[a] Tianjin Key Laboratory of Civil Structure Protection and Reinforcement, Tianjin Chengjian University, Tianjin, 300384, China
[b] School of Civil and Environmental Engineering, University of Technology Sydney, Sydney, NSW, 2007, Australia
[c] State Key Laboratory of Metastable Materials Science and Technology, Yanshan University, Qinhuangdao, 066000, China

ARTICLE INFO

Keywords:
3DP-UHPC
Hybrid fibre
Elevated-temperature
Interface bonding performance
Bonding strip

ABSTRACT

This study explored the influence of elevated-temperature exposure and interlayer time intervals on the interface bonding strength of hybrid-fibre 3D printed ultra-high-performance concrete (3DP-UHPC), and analysed the potential mechanisms driving these observed results. A relationship model for the bonding strength of hybrid fibre 3DP-UHPC in elevated-temperature environments was proposed. Results revealed that at 800 °C, localized damage occurred in 3DP-UHPC, but the addition of 0.5 % polypropylene fibres delayed the occurrence of spalling behaviour and enhanced its elevated-temperature resistance. Furthermore, as the time interval increased, the bonding strength of 3DP-UHPC gradually decreased, particularly at temperatures above 400 °C, where the melting and volatilization of polypropylene fibres negatively affected the bonding strength. The study suggested that polypropylene fibres inhibited spalling behaviour of 3DP-UHPC after elevated temperatures through moisture loss and thermal stability. However, they may also lead to interface weakening, resulting in a decrease in bonding strength. These findings provide important guidance for further development and design of 3DP-UHPC structures in elevated-temperature environments.

1. Introduction

In recent years, the rapid advancement of 3D printing technology has led to its wide application in various fields including architecture, manufacturing, and healthcare [1–3]. Concrete, as a crucial construction material, has also gained attention in the realm of 3D printing [4,5]. The technology of 3D printing concrete offers significant advantages such as the ability to create intricate shapes and customized designs, high processing efficiency, and optimal resource utilization [6–10]. Consequently, it finds suitability in numerous applications like constructing structural components, prefabricated residential buildings, bridges, and more.

With the increasing adoption of 3D printing concrete technology, there is a growing demand for materials with enhanced performance. Ultra-high performance concrete (UHPC) is an exceptional engineering material known for its superior characteristics, including enhanced crack resistance [11], higher strength [12,13], and excellent durability [14] as compared to conventional concrete. The outstanding durability of UHPC remarkably improves the lifespan of building structures while reducing the need for costly reinforcement and maintenance [15]. Moreover, its high toughness ensures greater reliability of concrete structures [16]. Consequently, 3DP-UHPC has become a captivating research area, drawing significant attention from scholars involved in 3D printing

* Corresponding author.
** Corresponding author.
E-mail addresses: Zhongxian1212@163.com (Z. Liu), Chengqing.wu@uts.edu.au (C. Wu).

https://doi.org/10.1016/j.jobe.2024.109801
Received 30 December 2023; Received in revised form 3 April 2024; Accepted 30 May 2024
Available online 1 June 2024

[17–19]. Scholars have conducted extensive studies on 3DP-UHPC, encompassing the development of unique formulae [17,20,21], exploration of microstructure and mechanical properties [18,20,22,23], and examination of durability aspects such as blast resistance [24] and frost resistance [25]. Additionally, some scholars have utilized 3DP-UHPC as a reinforcing material to strengthen 3D printed components made of ordinary concrete, successfully validating the effectiveness of this approach [26]. As a result, 3DP-UHPC exhibits immense potential for a wide range of applications. However, it is important to acknowledge that in practical applications, 3DP-UHPC, similar to conventional concrete, may experience extreme conditions such as fires and elevated-temperature industrial environments. Under such circumstances, the structure and performance of 3DP-UHPC can undergo changes, potentially leading to structural instability [27,28]. Elevated temperatures can result in thermal expansion, strength reduction, and material damage in 3DP-UHPC, consequently affecting the overall structural integrity [29,30]. While the unique formulation and fibre reinforcement technology of 3DP-UHPC may provide better resistance to elevated-temperature spalling in certain conditions as compared to traditional concrete, this does not imply that it possesses higher strength under all elevated-temperature conditions. In fact, previous studies [31] have indicated that after exposure to elevated temperatures, the compressive strength of 3DP-UHPC may be lower than that of traditional concrete. This strength variation is primarily attributed to the directional distribution of steel fibres and the presence of weak interfaces between layers in 3DP-UHPC. These characteristics play a crucial role in enhancing resistance to elevated-temperature spalling but can also lead to anisotropy in compressive strength. Therefore, investigating the behaviour of 3DP-UHPC following exposure to elevated temperatures holds great significance in designing safer and more reliable building structures, as well as ensuring the secure operation of buildings in extreme situations like fires.

The previous study [31] observed that existing 3DP-UHPC materials possess a certain resistance to elevated temperatures. To enhance its performance under elevated-temperature conditions, the authors conducted an extensive review of relevant literature. From the reviewed studies, it was found that polypropylene fibres have a positive impact on improving the toughness, crack resistance, and elevated-temperature resistance of concrete materials [29,32,33]. When concrete is exposed to elevated-temperature environments, polypropylene fibres can effectively absorb and disperse thermal stress, thereby reducing the temperature gradient within the concrete and decreasing the risk of material cracking. In addition, polypropylene fibres can provide reinforcement effects, increasing the strength and durability of the concrete. Therefore, in this study, the authors chose to add 0.5 % by volume of polypropylene fibres to the existing 3DP-UHPC formulation to further enhance the material's performance under elevated-temperature conditions. Additionally, the authors have identified that the interface bonding strip, which refers to the layer-to-layer interfacial regions in 3DP-UHPC, significantly influences the material's resistance to elevated temperatures. Firstly, in elevated-temperature environments, these interfacial regions may exhibit weaknesses that can lead to issues such as reduced bonding strength, crack propagation, and concentration of thermal stress. Secondly, variations in factors like structural morphology, setting parameters, and printing material characteristics in 3D printing construction can result in different interlayer time intervals. Prolonging the interlayer time interval can adversely affect the quality of the bonding strip in 3DP-UHPC, leading to increased porosity and reduced compactness [34]. These effects are likely to be exacerbated under elevated-temperature conditions. Despite the clear impact of these factors, there has been a lack of investigation into the interface bonding characteristics of 3DP-UHPC following exposure to elevated temperatures, which is an area that warrants further research. It is also important to thoroughly consider the impact of interlayer time intervals on the interface bonding performance of 3DP-UHPC after elevated temperatures.

In this study, the interface bonding characteristics of hybrid fibre 3DP-UHPC under different conditions were investigated. Microstructure analysis and bonding strength tests were conducted on specimens treated at room temperature (20 °C) and elevated temperatures ranging from 200 to 800 °C. The influence of interlayer time interval and elevated temperature on the bonding characteristics of hybrid fibre 3DP-UHPC was also examined. To compare the bonding performance differences between 3D printed concrete and traditional mould-casting concrete, a control group using mould-casting ultra-high performance concrete (MC-UHPC) with varying pouring time intervals was included. Based on the findings, a proposed model was developed to describe the relationship between the interface bonding strength of hybrid fibre 3DP-UHPC and its exposure to elevated temperatures. The aim of this study is to offer valuable guidance for enhancing the elevated-temperature resistance of 3D printed buildings.

2. Experimental designs

2.1. Materials

UHPC is an important building engineering material, with mechanical properties and durability indicators much more superior than ordinary concrete. Therefore, it is necessary to strictly select materials in accordance with the standard "Technical Requirements for Ultra High Performance Concrete (UHPC)" T/CECS 10107-2020 [35]. The experimental materials comprised cement, silica fume, fly ash, quartz sand, nano calcium carbonate, cellulose, polycarboxylate superplasticizer, water, steel fibre, and polypropylene fibre. The steel and polypropylene fibres, detailed in Tables 1 and 2, were chosen for reinforcement in the 3DP-UHPC, providing robust interfacial bonding and enhanced durability. The mix proportion, presented in Table 3, was carefully designed to optimize the workability and mechanical properties of the 3DP-UHPC. Notably, the mixture ratio for MC-UHPC is identical to that of the 3DP-UHPC to ensure a consistent baseline for comparison. The selection of materials and the precise mix design are crucial for achieving the

Table 1
Main physical parameters of steel fibres.

Length (mm)	Diameter (mm)	Density (g/cm^3)	Form	Tensile strength (MPa)
6	0.12	7800	Bright circular	>2500

Table 2
Main technical parameters of polypropylene fibres.

Length (mm)	Diameter (μm)	Specific gravity	Melting point (°C)	Tensile strength (MPa)	Elastic modulus (GPa)	Tensile limit (%)
10	31	0.91	160–169	>486	>4.8	>15 %

Table 3
Proportion of mix (kg/m^3).

Materials	3DP-UHPC
Cement	750
Silica fume	165
Fly ash	165
Fine sand	540
Medium sand	360
Coarse sand	180
Nano calcium carbonate	24
Cellulose	1.08
Polycarboxylate superplasticizer	10
Water	154
Steel fibre	78
Polypropylene fibre	4.5

desired properties in the final UHPC product. The silica fume and fly ash, for example, contribute to the pozzolanic reaction, enhancing the strength and durability of the concrete. The addition of nano calcium carbonate aims to improve the packing density and refine the microstructure of the UHPC. The cellulose and polycarboxylate superplasticizer were chosen for their effectiveness in enhancing the workability of the mix without compromising the strength. In this study, steel and polypropylene fibres were selected for 3DP-UHPC reinforcement, with properties detailed in Tables 1 and 2 The 6-mm steel fibres, with >2500 MPa tensile strength, offer robust interfacial bonding and enhanced toughness. Their bright circular shape and untreated surface improve crack resistance without coatings. The 10-mm polypropylene fibres, with >486 MPa tensile strength and >4.8 GPa elastic modulus, ensure stress distribution and durability, with their thermal resistance (160–169 °C melting point) crucial for elevated-temperature performance.

2.2. Specimen preparation and size

At present, there are roughly three testing methods for the bonding strength of 3D printed concrete interfaces: interlayer tensile, shear, and splitting test. Considering the mature development of interlayer tensile testing and referring to the research of some scholars [36–38], this study chose to use interlayer tensile testing to explore the interface bonding behaviour of hybrid fibre 3DP-UHPC. The HC1008 desktop concrete 3D printer for printing, with a circular nozzle and a diameter of 15 mm was used. According to the size of the printer nozzle, the 3DP-UHPC specimen was selected as a rectangular shape with a size set to 15 × 15 × 10 mm.

By mixing and stirring various materials, the fresh mortar required for the experiment was obtained. The slump flow diameter of the fresh mortar was 174 ± 3 mm, within the typical range required for printable concrete (150–190 mm) [39], which means that fresh mortar had suitable flowability and plasticity, meeting the requirements for 3D printing. Before obtaining the experimental 3DP-UHPC specimen, a 3D printer was used to prepare the large specimen as shown in Fig. 1(b) according to the Cura software model design in Fig. 1(a). During the printing process, different interlayer time intervals were achieved by controlling the printing speed, and the initial extrusion speed was set to 0.4 mm/s. Considering the impact of the printing process, in order to ensure the stability of the printing wire size, the extrusion speed was adjusted according to the changes in printing speed throughout the entire printing process. In accordance with the "Standard for Testing Methods for Physical and Mechanical Properties of Concrete" GB/T 50081-2019 [40], after 28 days of curing, the large specimens were cut and separated to obtain the required test pieces (see Fig. 2).

In order to maximize the assumption of uniformity and make the lateral cutting cross section as perpendicular as possible to the upper and lower surfaces, the surfaces of the 3DP-UHPC specimens with dimensions of 15 × 15 mm were polished. Meanwhile,

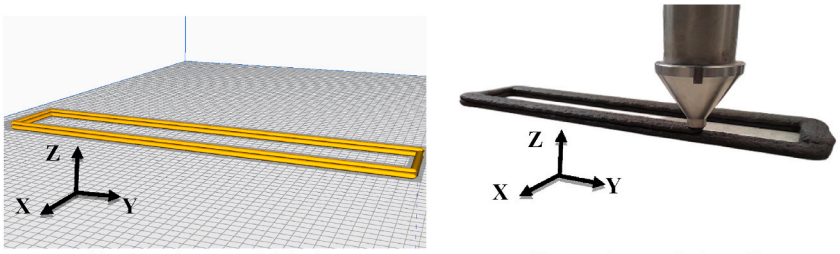

(a) 3D printer model design (b) Specimen printing effect

Fig. 1. Preparation of 3D printed large specimens.

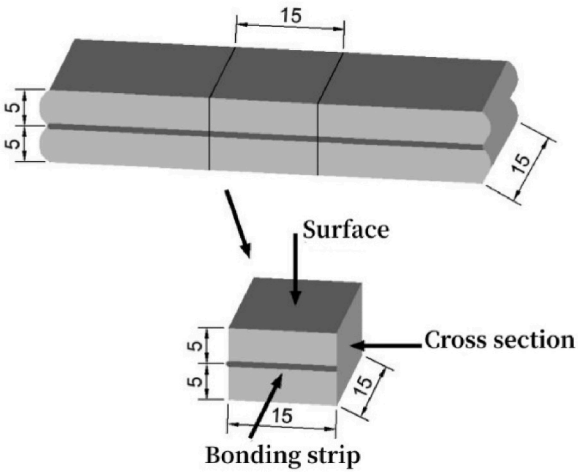

Fig. 2. Preparation of 3DP-UHPC specimens.

reference specimens MC-UHPC were prepared for comparison. Referring to GB/T 16777-2008 ″Test Methods for Building Waterproof Coatings" [41], the MC-UHPC specimens were prepared using an 8-shaped mould with dimensions of 78 × 22.5 × 22.5 mm. Prior to pouring, the iron sheet was inserted into the central groove of the 8-shaped mould. In order to achieve different pouring time intervals in the experimental design, the pouring process was divided into two batches for each part. Following the completion of pouring, an iron sheet was extracted to simulate the bonding strip of 3DP-UHPC. No treatment was applied to the bonding strip. Fig. 3(a) illustrates the configuration of the 8-shaped mould and iron sheet, while Fig. 3(b) showcases the pouring effect. To ensure consistency in the experiment, the pouring time interval of MC-UHPC specimens with a 0 min interval was also carried out using the same method to avoid fibres passing through the bonding strip. It should be noted that the extraction of an iron sheet may not fully represent the layer-by-layer deposition process of actual 3D printing. However, due to limitations in the experimental setup and available resources, the authors chose this pouring method for MC-UHPC specimens as a practical approximation. While it may not capture all the complexities of the 3D printing process, the authors believe that this approach still provides valuable insights into the performance of the bonding strip in MC-UHPC.

In this experiment, the specimens were divided into five categories based on the target temperature, namely 20 °C, 200 °C, 400 °C, 600 °C, and 800 °C. The maximum temperature satisfied the minimum temperature requirements specified in ISO 834 standard [42]. According to the preparation method, it was divided into two categories: 3DP-UHPC and MC-UHPC. Based on different preparation methods and process characteristics, time intervals were set. For 3DP-UHPC, in order to optimize parameters and quickly evaluate the performance of 3DP-UHPC materials after elevated-temperature treatment, as well as obtain feasible results within a limited time, it could be classified into three categories based on the interlayer time interval, namely 0.5 min, 2 min, and 5 min; for MC-UHPC, to be sure that the concrete can fully fill the mould during the pouring process, ensuring the quality and uniformity of the casting, and considering the need for certain detail treatments or addition of special materials, it may be necessary to extend the pouring time interval to complete the related operations. Based on the pouring time interval, it was divided into six categories, namely 0 min, 5 min, 10 min, 30 min, 60 min, and 1 day.

To distinguish different types of specimens, the specimens were labelled using the a-b-c format. Among them, "a" refers to the two preparation methods of 3D printing and mould-casting, represented by 3D and MC, respectively; "b" denotes different time intervals, represented by "0.5", "2", and "5" for 3DP-UHPC, and "0", "5", "10", "30", "60", and "1d" for MC-UHPC; "c" refers to different target temperatures, represented by "20", "200", "400", "600", and "800", respectively. All specimens were divided into 45 categories, with 3 duplicated specimens prepared for each category. The microstructure was observed firstly, and then mechanical performance tests

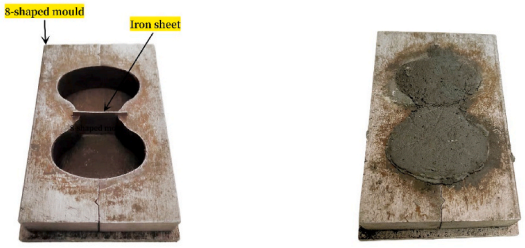

(a) 8-shaped mould with iron sheet (b) 8-shaped mould after pouring

Fig. 3. Examples of 8-shaped mould.

were conducted. The labels for each type of specimen are summarized in Table 4.

2.3. Experimental setup

2.3.1. Elevated-temperature heating test

In this experiment, authors employed an SSJ-14T rapid thermal rise box furnace for the heating process, which can reach an internal maximum temperature of 1400 °C with a temperature control accuracy of ±1 °C and a temperature uniformity of ±8 °C (in an empty furnace state, within the effective temperature zone of the furnace cavity). The heating rate (4 °C/min) and constant temperature time (2 h) consistent with previous research [31] were used. The specific temperature rise curve is presented in Fig. 4. A total of 135 specimens participated in the elevated-temperature heating test.

2.3.2. Bonding performance test

In accordance with the requirements of GB/T 16777-2008 ″Test Methods for Building Waterproof Coatings” [41], the bonding strength test was conducted on the UTM5202 electronic universal testing machine, with an accuracy grade of 0.5, as shown in Fig. 5(a). To obtain the tensile strain of the bonding performance of specimens, resistance strain gauges were installed on different types of specimens and strain data were collected using the JM3811 static strain testing system, as depicted in Fig. 5(b). The static strain testing system had a gauge factor sensitivity of 1.0–3.0 with automatic correction and a system accuracy of ±0.3 % Fs ± 2με.

Fig. 6 displays the bonding strength test setup. Prior to the experiment, strain gauges were attached to the interface bonding strip of the 3DP-UHPC specimens on the side with dimensions of 15 × 10 mm using epoxy resin AB glue, ensuring that the strain gauges were perpendicular to the bonding strip and had a strong adhesion with the specimens. Prior to the attachment of the strain gauges, a

Table 4
Classification of microstructure and bonding test specimens for 3DP-UHPC after elevated temperature.

Preparation method	Time interval	Target temperature	Specimen label
3DP-UHPC	0.5 min	20 °C	3D-0.5-20
		200 °C	3D-0.5-200
		400 °C	3D-0.5-400
		600 °C	3D-0.5-600
		800 °C	3D-0.5-800
	2 min	20 °C	3D-2-20
		200 °C	3D-2-200
		400 °C	3D-2-400
		600 °C	3D-2-600
		800 °C	3D-2-800
	5 min	20 °C	3D-5-20
		200 °C	3D-5-200
		400 °C	3D-5-400
		600 °C	3D-5-600
		800 °C	3D-5-800
MC-UHPC	0 min	20 °C	MC-0-20
		200 °C	MC-0-200
		400 °C	MC-0-400
		600 °C	MC-0-600
		800 °C	MC-0-800
	5 min	20 °C	MC-5-20
		200 °C	MC-5-200
		400 °C	MC-5-400
		600 °C	MC-5-600
		800 °C	MC-5-800
	10 min	20 °C	MC-10-20
		200 °C	MC-10-200
		400 °C	MC-10-400
		600 °C	MC-10-600
		800 °C	MC-10-800
	30 min	20 °C	MC-30-20
		200 °C	MC-30-200
		400 °C	MC-30-400
		600 °C	MC-30-600
		800 °C	MC-30-800
	60 min	20 °C	MC-60-20
		200 °C	MC-60-200
		400 °C	MC-60-400
		600 °C	MC-60-600
		800 °C	MC-60-800
	1 d	20 °C	MC-1d-20
		200 °C	MC-1d-200
		400 °C	MC-1d-400
		600 °C	MC-1d-600
		800 °C	MC-1d-800

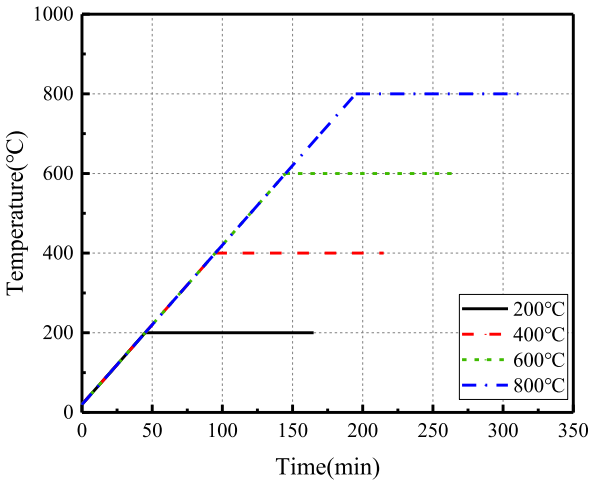

Fig. 4. Temperature rise curve of elevated-temperature heating test.

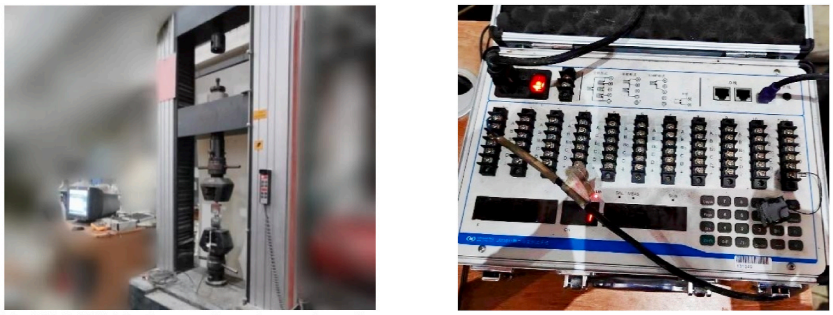

(a) UTM5202 electronic universal testing machine

(b) JM3811 static strain testing system

Fig. 5. Bonding strength measuring instrument.

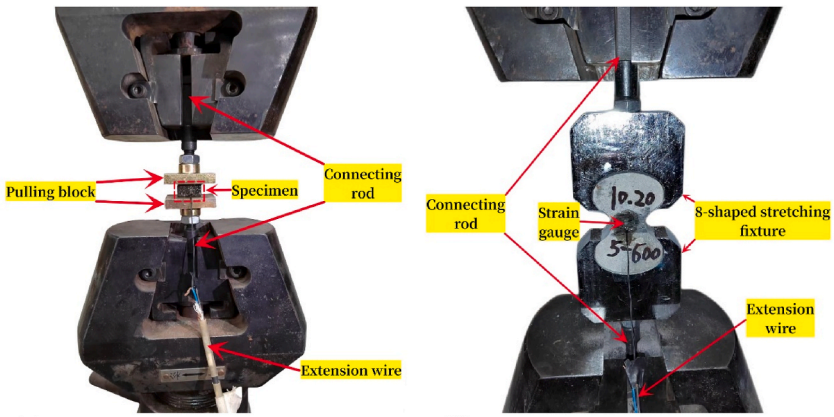

(a) 3DP-UHPC bonding performance test setup

(b) MC-UHPC bonding performance test setup

Fig. 6. Bonding performance test setup.

thorough inspection was conducted to minimize the presence of noticeable cracks near the bonding strip. This was done to minimize any potential interference from cracks on the experimental results and to ensure the accuracy of the collected data. In addition, epoxy resin AB glue was used to bond the two end faces of the 3DP-UHPC specimens with dimensions of 15 × 15 mm to the threaded pull-out blocks with dimensions of 50 × 50 mm. During the bonding process, the two end faces were fully aligned with the pull-out blocks and

the centre points of the specimens and the pull-out blocks were on the same vertical line to ensure uniform tension during the experiment. After the adhesive was fully cured, the pull-out blocks were tightened with the connecting rods, and the strain gauges were connected to the strain testing system via extension wires. The specimens were then mounted onto the testing machine for the test, as shown in Fig. 6(a). For MC-UHPC, the 8-shaped stretching fixture was installed on the testing machine to perform the test, as shown in Fig. 6(b). Strain gauges were also attached to the bonding strip of MC-UHPC specimens to measure the tensile strain of different specimens. The testing machine applied a displacement control speed of 0.2 mm/min for loading. A total of 45 3DP-UHPC specimens were tested for bonding tensile strength, while 90 MC-UHPC specimens were tested in the same manner.

2.3.3. Scanning electron microscope test

Scanning electron microscope (SEM) provides powerful tools and means for studying the microscopic characteristics, hydration processes, and phase transitions of cement-based materials. In this experiment, small thin specimens with a length and width of less than 5 mm and a thickness of less than 1 mm were extracted from 3DP-UHPC specimens subjected to different temperatures. After drying, the specimens were observed using a JSM-7800F field emission scanning electron microscope, with a resolution of 1.2 nm. There were a total of 5 specimens.

2.3.4. Observation test of bonding strip

Specimens measuring approximately 15 mm in length, 10 mm in width, and 10 mm in height were extracted from both 3DP-UHPC and MC-UHPC specimens. The changes in the bonding strip between 3DP-UHPC and MC-UHPC were observed using the VHX-600E ultra depth of field 3D display system at different time intervals and temperatures, as depicted in Fig. 7. This system is equipped with a 2.11-megapixel CCD sensor measuring 1/1.8 inch. A total of 15 3DP-UHPC specimens and 30 MC-UHPC specimens were observed, respectively.

3. Results and discussion

3.1. Elevated-temperature test phenomena and SEM analysis

3.1.1. The phenomena of elevated-temperature testing on UHPC

As a heterogeneous mixture, UHPC has a three-phase coexistence of solid, liquid, and gas. Elevated-temperature action can change its phase composition, causing a series of physical and chemical changes inside, thereby affecting the appearance and quality of UHPC. The changes in the appearance of all specimen types with increasing temperature are illustrated in Tables 5 and 6. It was noted that as the temperature increases, the apparent colour of the specimen changed from dark to light, and then gradually became darker. Some specimens exhibited peeling phenomenon and local damage under the elevated-temperature of 800 °C, which delayed the occurrence of cracking as compared to reference [31]. This is because the polypropylene fibres added melted after reaching the melting point. As the temperature continued to rise to the vaporization temperature of the polypropylene fibres [43], the liquid polypropylene fibres gradually evaporated, leaving microchannels for UHPC. Water inside UHPC could migrate along the microchannels and evaporate to the outside of UHPC, relieving the steam pressure inside the UHPC and preventing it from bursting attributable to steam pressure [44]. Several scholars have also reached similar conclusions [45–47]. In addition, it was pointed out that polypropylene fibres cause microcracks inside the concrete before melting, which can provide channels for relieving pore pressure [48,49]. This may also be one of the reasons why polypropylene fibres delay UHPC elevated-temperature cracking.

When analysing the ignition loss rate and its correlation with temperature for hybrid fibre 3DP-UHPC and MC-UHPC, it is important to understand the significance of this analysis in terms of evaluating UHPC's behaviour and properties in elevated-temperature environments. By assessing ignition loss, researchers can better understand the material changes and quality losses that occur in UHPC after elevated temperatures, providing a more comprehensive understanding of UHPC's performance and property changes in elevated-temperature environments.

In this study, the addition of 0.5 % polypropylene fibre successfully delayed cracking during the heating process of both 3DP-UHPC and MC-UHPC, enhancing their resistance to elevated temperatures. Fig. 8 depicts the correlation between the ignition loss rate and temperature for hybrid fibre 3DP-UHPC and MC-UHPC. The correlation between ignition loss rate and temperature was found to be significant in determining UHPC's behaviour and properties after elevated temperatures. The melting point and vaporization

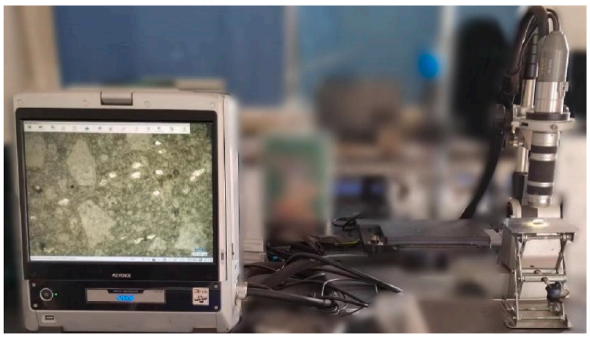

Fig. 7. Bonding strip observation instrument.

Table 5
Appearance of 3DP-UHPC specimens after elevated-temperature cooling.

Label	20°C	200°C	400°C	600°C	800°C
3D-0.5					
3D-2					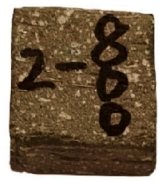
3D-5					

temperature of the polypropylene fibres played a critical role in UHPC's reaction to heat [43], with the vaporization and volatilization of polypropylene fibres creating effective channels for internal water loss in concrete. This resulted in the formation of numerous micropores that facilitated water migration and loss, contributing to the increase in burning loss rate after 400 °C. The weak surface interface of the 3DP-UHPC specimen also allowed water vaporing to escape more easily, contributing to slightly higher ignition loss rates after 400 °C as compared to MC-UHPC. The burning loss rate of the specimens continued to rise within the elevated temperature range of 400–800 °C due to the dehydration and decomposition of the C-S-H gel and $Ca(OH)_2$ present. However, at the target temperature of 600 °C and 800 °C, the concrete matrix began to exhibit looseness and porosity, and the negligible effect of the weak surface interface on water evaporation explains why the burning loss rates of 3DP-UHPC and MC-UHPC were almost identical. However, by comparing the ignition loss rates of 3DP-UHPC and MC-UHPC with reference [31], it was observed that the hybrid fibre specimen demonstrated almost no difference in ignition loss rate at the desired temperature of 200 °C as compared to the singly doped steel fibre specimen. This was ascribed to the fact that the melted polypropylene fibre did not introduce additional pores into UHPC. After 200 °C, which exceeded the melting point but was below the vaporization temperature of polypropylene fibres, part of the melted polypropylene fibres was absorbed by the surrounding pores slurry, without significant changes in the total porosity inside the concrete. Experimental studies have demonstrated this observation [43,50].

Overall, the addition of 0.5 % polypropylene fibre successfully delayed cracking during the heating process of 3DP-UHPC and MC-UHPC, and enhanced their resistance to elevated temperatures. These findings have significant implications for the design and construction of 3DP-UHPC structures, particularly in real-world scenarios where such structures are subjected to elevated temperatures. The enhanced resistance to spalling behaviour and improved elevated-temperature performance, attributed to the addition of 0.5 % polypropylene fibres, suggesting that 3DP-UHPC can be effectively utilized in environments prone to fires or elevated temperatures, such as industrial settings or regions with extreme climatic conditions.

3.1.2. SEM analysis

In order to analyse the effect of temperature on the macroscopic experimental phenomena of hybrid fibre 3DP-UHPC from a microscopic perspective, SEM was used to observe the microstructure of the matrix and matrix fibre interface transition zone (ITZ) at the bonding strip of 3DP-UHPC after different temperatures. The results are listed in Table 7. It should be noted that the matrix and ITZ of MC-UHPC are not different from 3DP-UHPC, and the microscopic analysis results in this experiment are also applicable to MC-UHPC.

As shown in Table 7 A1, the microstructure of 3DP-UHPC at 20 °C consisted of granular C-S-H gel, hexagonal plate-like $Ca(OH)_2$ (CH phase), and unhydrated fly ash particles. Hot bath curing at 90 °C accelerated the pozzolanic reaction of mineral admixtures such as silica fume and fly ash. This reaction consumed $Ca(OH)_2$ and generated compact C-S-H gel, which filled the pores tightly, resulting in a complete and compact matrix. Consequently, the mechanical properties of 3DP-UHPC bonding strip were improved [51,52]. At 20 °C, the presence of polypropylene fibres can be clearly observed under a microscope, and the ITZ zone fibres are tightly bonded to the matrix, as shown in Table 7 A2. The microstructure of the 3DP-UHPC matrix treated after 200 °C did not show significant changes in contrast to 20 °C, as demonstrated in Table 7 B1. However, fibrous polypropylene fibres were no longer observed. The ITZ between

Table 6
Appearance of MC-UHPC specimens after elevated-temperature cooling.

Label	20°C	200°C	400°C	600°C	800°C
MC-0					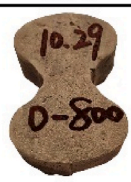
MC-5					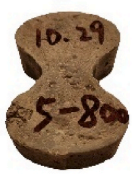
MC-10					
MC-30					
MC-60					
MC-1d					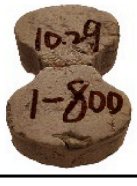

the steel fibres and the matrix remained tight, as shown in Table 7 B2. Table 7 C1 displays the microstructure of the 3DP-UHPC matrix following treatment after 400 °C. In contrast to the specimen treated after 200 °C, the content of C-S-H gel was noticeably higher. The cement hydration reaction resulted in a more compact matrix structure and a decrease in CH crystals. Furthermore, there were no observable particles of unhydrated fly ash. The difference in thermal expansion coefficient between polypropylene fibres and concrete caused microcracks in the concrete around the polypropylene fibres as the fibres expanded before melting. These cracks created fibrous pores in the matrix [53]. Pores could be observed in Table 7 C2, and the ITZ between the steel fibres and the matrix weak end after 400 °C. Oxidative decarburization occurred on the surface of steel fibres. After 600 °C, the particle-like C-S-H gel became significantly less and more dispersed in the matrix. Obvious cracks appeared in the matrix, likely owing to stress caused by the mismatch of the thermal expansion coefficient between the steel fibres and the matrix, as shown in Table 7 D1. ITZ became loose, cracks further expanded, and the surface oxidation and decarburization of steel fibres intensified, as displayed in Table 7 D2. After 800 °C, a significant amount of fibrous or sheet-like substances, inferred to be tobermorite, were observed in the concrete matrix. C-S-H gel formed by the aggregation of disordered calcium silicate hydrates rearranged its crystal structure under elevated-temperature or high-pressure conditions, forming a more stable tobermorite structure [54]. Studies indicated that tobermorite could transform into dehydroxylated tobermorite when the temperature rose to 724 °C, resulting in the breakage of some *Si*-O-H bonds [55]. Dehydroxytobermorite, typically presenting a fibrous or sheet-like morphology, was a transition phase from low-temperature to elevated-temperature wollastonite, as shown in Table 7 E1. Based on the observations in Table 7 E2, it was apparent that the bond between the steel fibre and the matrix was completely severed. The surface of the steel fibre underwent complete deoxidization and carbonization,

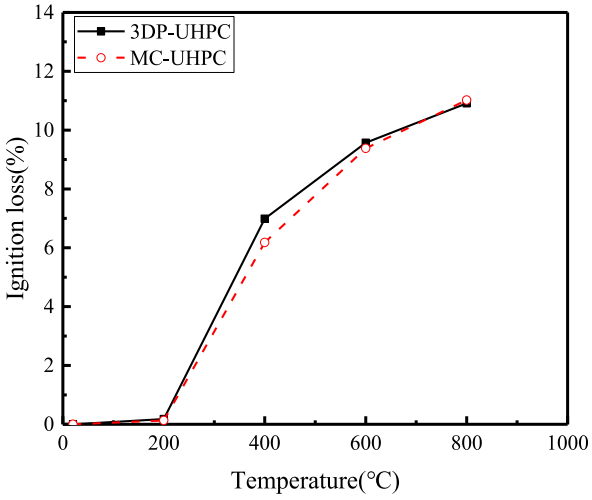

Fig. 8. Relationship between ignition loss rate and temperature of 3DP-UHPC and MC-UHPC.

making it susceptible to fracture. As a result, the strength of 3DP-UHPC bonding strip was nearly lost.

Furthermore, the SEM analysis provides insights into the microstructural changes that can inform the design of 3DP-UHPC components for real-world applications. The observed microcracks and degradation of the steel fibre interface under elevated temperatures are critical factors to consider when designing structures that will be exposed to extreme conditions, such as in fire-resistant construction or areas with high thermal stress. These findings suggest the need for careful material selection and process optimization to ensure the long-term performance and safety of 3DP-UHPC structures.

3.2. Experimental results and analysis of microstructure of bonding strip after elevated temperature

Unlike traditional concrete construction techniques, 3D printing has a unique strip by strip stacking technology, which enables 3D printed concrete components to have interlayer bonding strip. When subjected to force, 3D printed components will experience stress concentration and damage due to interface junctions, thereby affecting their own bearing capacity and durability [56]. Reference [31] also pointed out that the weakness of the interface bonding strip could affect the elevated-temperature resistance of 3DP-UHPC. Therefore, considering factors such as temperature and interlayer time interval, a specific analysis was conducted on the microstructure of the bonding strip after elevated-temperature treatment of 3DP-UHPC and MC-UHPC, and the differences in the microstructure of the bonding strip after elevated-temperature treatment were analysed from the perspective of pouring methods. The microstructure images of the bonding strip after elevated-temperature treatment of all types of specimens are shown in Table 8.

3.2.1. The effect of temperature on the microstructure of the bonding strip after elevated temperature

Table 8 demonstrates that the tightness of the bonding strip in all specimen types initially increased and then decreased as the target temperature rose. Starting after 200 °C, there was minimal change in the tightness of the bonding strip compared to that at 20 °C. As previously indicated, any pores formed due to the melting and absorption of polypropylene fibres or the evaporation of free water in the bonding strip did not have a significant impact on the tightness of the bonding strip in UHPC specimens. The heating process instead facilitated the secondary hydration reaction of cement. The pozzolanic reaction of silica fume and fly ash consumed $Ca(OH)_2$ in the bonding strip and generated C-S-H gel, which resulted in a denser bonding strip. However, since the temperature did not differ significantly from the hot water bath curing temperature, the pozzolanic reaction during the calcination process was not sufficient to cause remarkable changes in the compactness of the bonding strip in contrast to that at 20 °C. Therefore, the overall effect was in limited improvement in bonding strength. After being exposed to 400 °C, the cement hydration reaction persisted and resulted in a rise in the volume density of C-S-H gel within the cement matrix. This increase effectively filled the bonding strip, leading to a positive impact on the bonding strength [57]. However, as observed from Table 8, the melting and volatilization of polypropylene fibres created a large number of voids, which could form a connected pore structure with the original pores containing free water and capillary water. The elevated temperature also damaged the pore structure, resulting in an increase in the pore volume of the bonding strip, which had a negative effect on bonding strength [43]. Based on the experimental results, it could be concluded that the negative effect dominated after 400 °C, causing the bonding strength to be slightly lower than that after 200 °C. As the temperature increased to 400–800 °C, although there was still a positive effect from the ongoing cement hydration reaction, the matrix lacked unhydrated spherical gel particles, and the positive effect reached a plateau. Meanwhile, the elevated temperature led to further dehydration and decomposition of C-S-H gel, which enlarged the pores in the bonding strip. Microcracks gradually widened and penetrated, forming bonding joints and resulting in a significant loss of macro bonding performance. The damage to the matrix caused by the elevated temperature continued to increase [57].

In addition, it could be observed in Table 8 that MC-60 and MC-1d after lower target temperatures formed a white boundary at the bonding strip. Based on the research of other scholars [58], the authors speculated that this white boundary was a thin strip of water

Table 7
SEM images of 3DP-UHPC matrix and ITZ.

	Matrix	ITZ
20°C	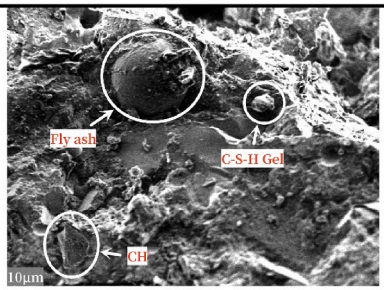 A1: 3DP-UHPC at room temperature	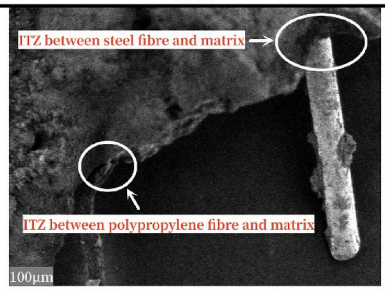 A2: 3DP-UHPC at room temperature
200°C	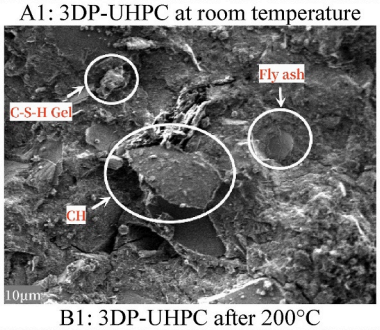 B1: 3DP-UHPC after 200°C	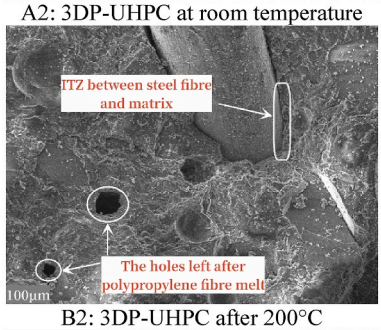 B2: 3DP-UHPC after 200°C
400°C	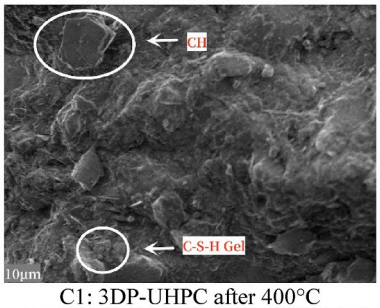 C1: 3DP-UHPC after 400°C	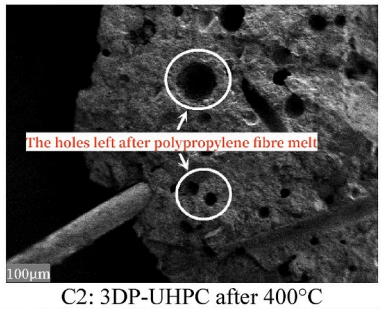 C2: 3DP-UHPC after 400°C
600°C	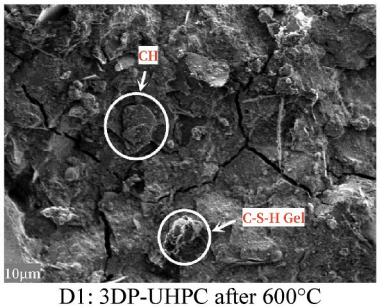 D1: 3DP-UHPC after 600°C	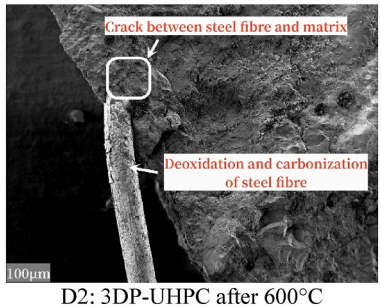 D2: 3DP-UHPC after 600°C
800°C	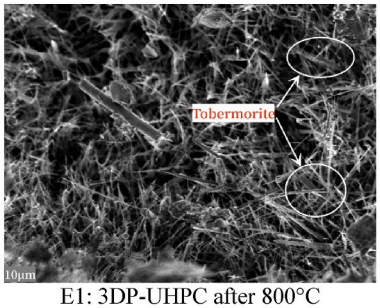 E1: 3DP-UHPC after 800°C	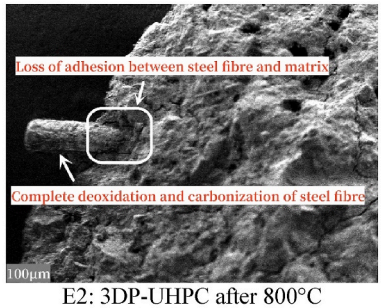 E2: 3DP-UHPC after 800°C

Table 8
Microscopic images of bonding strips of all types of specimens after elevated temperature.

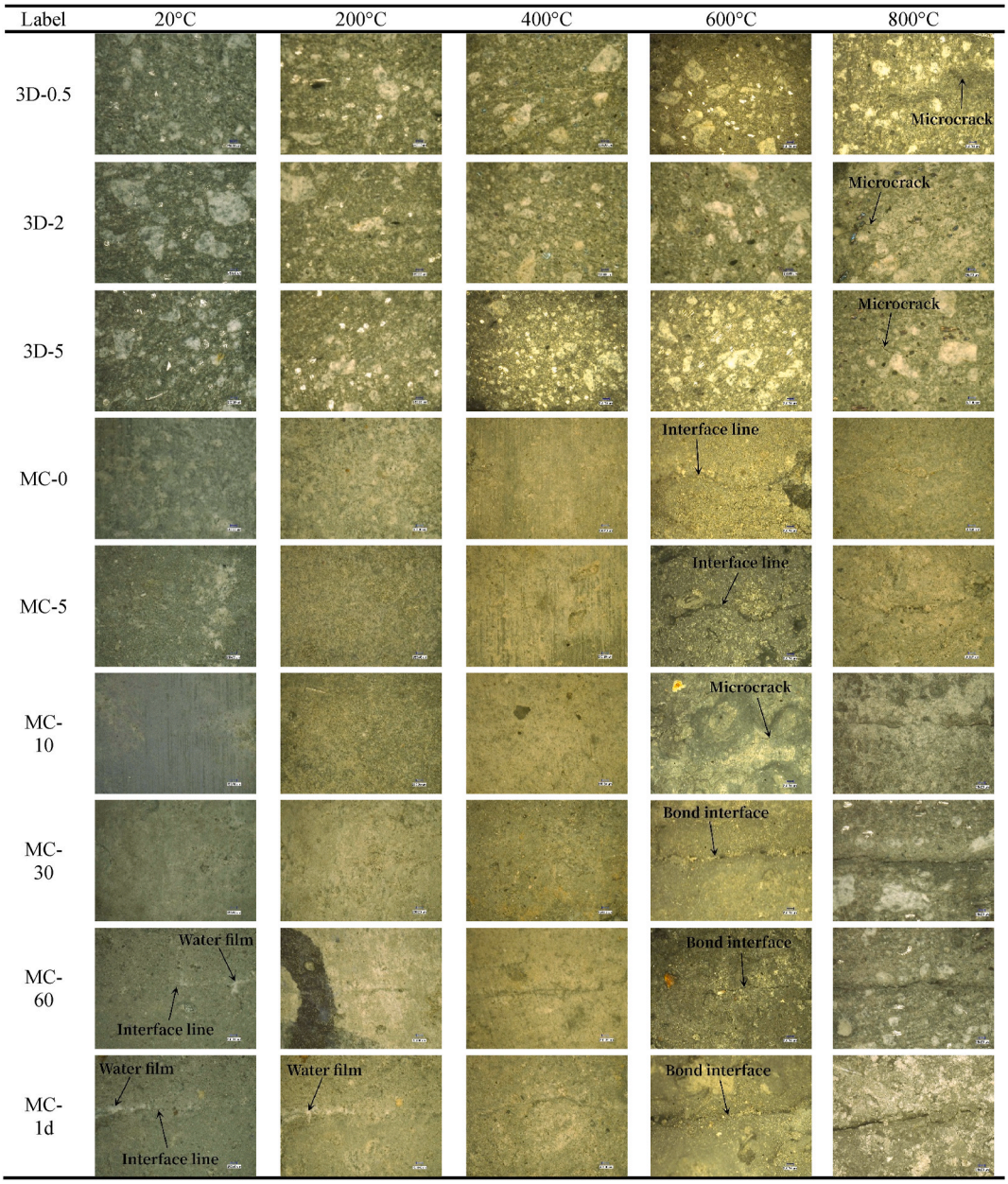

film, which might be related to the strong hydrophilicity of old concrete, leading to an increase in the water cement ratio of the bonding strip and the generation of more high-strength crystals such as $Ca(OH)_2$. As the target temperature increased, the water gradually evaporated, causing the water film to gradually disappear.

3.2.2. The effect of interlayer time interval on the microstructure of bonding strip after elevated temperature

In this study, the authors focused on the effect of interlayer time interval on the microstructure of the bonding strip after elevated temperature, which was an important indicator [59,60]. The interlayer time interval referred to the time interval between placing the second strip of concrete on it beyond a certain delay time after the first strip of concrete was poured. The authors found that the length of this time interval directly affected the microstructure of the bonding strip after elevated temperature.

According to Tables 8 and it could be observed that for 3DP-UHPC, there was no significant difference in the presence of microcracks between different interlayer time intervals after temperatures ranging from 20 to 600 °C. However, when subjected to a temperature of 800 °C, the microcracks formed by 3DP-UHPC gradually became more apparent with longer interlayer time intervals.

In the case of MC-UHPC, as the time interval increased, the observation of specimens at the boundary became increasingly clear within the temperature range of 20–400 °C. Even after 600 °C, the specimen with the shortest time interval (MC-0-600) clearly exhibited the boundary. As the time interval continued to increase, microcracks gradually appeared around the boundary and expanded to form adhesive joints. This phenomenon could be attributed to the escape of water and bubbles from inside UHPC towards the concrete surface as the time interval increases. This results in settlement and shrinkage on the concrete surface. Owing to differences in settlement and shrinkage between new and old concrete, the bonding quality of MC-UHPC along the height direction became uneven. Weaker bonding strength, defected such as voids and holes, and uneven bonding surfaces were observed. After elevated temperatures (e.g., 600 °C and 800 °C), these areas experienced greater thermal expansion, leading to localized temperature stress concentration. This concentration of temperature stress could initiate and propagate microcracks within the material, which might eventually evolve into bonding joints, cracks, or even failure [61]. Table 8 also shows a similar phenomenon at 800 °C, where specimens with different time intervals exhibited significant degradation as compared to those after 600 °C.

3.2.3. The effect of pouring method on the microstructure of bonding strip after elevated temperature

To make a fair comparison of the microstructure of the bonding strip between MC-UHPC and 3DP-UHPC after elevated temperature exposure, only MC-0 and MC-5 specimens were selected for comparison with 3DP-UHPC. Based on the images provided in Tables 8 and it could be observed that the microstructure of the bonding strip in 3DP-UHPC was more compact in comparison with MC-UHPC after different temperatures. Specifically, after 600 °C, a clear boundary could be seen between MC-0 and MC-5 specimens. This could be attributed to the escape of moisture and bubbles under elevated temperatures in MC-UHPC, which led to surface settlement and shrinkage of the concrete and the formation of cracks and pores in the bonding strip. In contrast, 3DP-UHPC exhibited a more uniform structure, and no distinct boundary could be observed in its bonding strip after 600 °C. This difference could be attributed to the preparation process of MC-UHPC and 3DP-UHPC. During the 3D printing process, the extrusion effect of the nozzle enhanced the compaction of the bonding strip in 3DP-UHPC [62,63]. As a result, in elevated-temperature environments, the microstructure of the bonding strip in 3DP-UHPC remained relatively stable and exhibited higher levels of compactness. This enhanced microstructure provided better load-bearing capacity and crack resistance, which might result in a longer service life and more reliable performance in practical applications.

The enhanced microstructure of 3DP-UHPC, attributed to the controlled 3D printing process, offers practical advantages for constructing robust structures, particularly in harsh thermal environments. This insight underscores the value of optimizing 3D printing parameters to ensure superior interlayer bonding and structural performance in real-world applications. The findings on the coupling effects of interlayer time intervals and elevated temperatures further inform construction planning, highlighting the need to balance curing times for optimal bonding and structural integrity. By doing so, 3DP-UHPC can be effectively utilized to create durable infrastructure with improved safety and reduced maintenance needs. In summary, the analysis of 3DP-UHPC's microstructure and

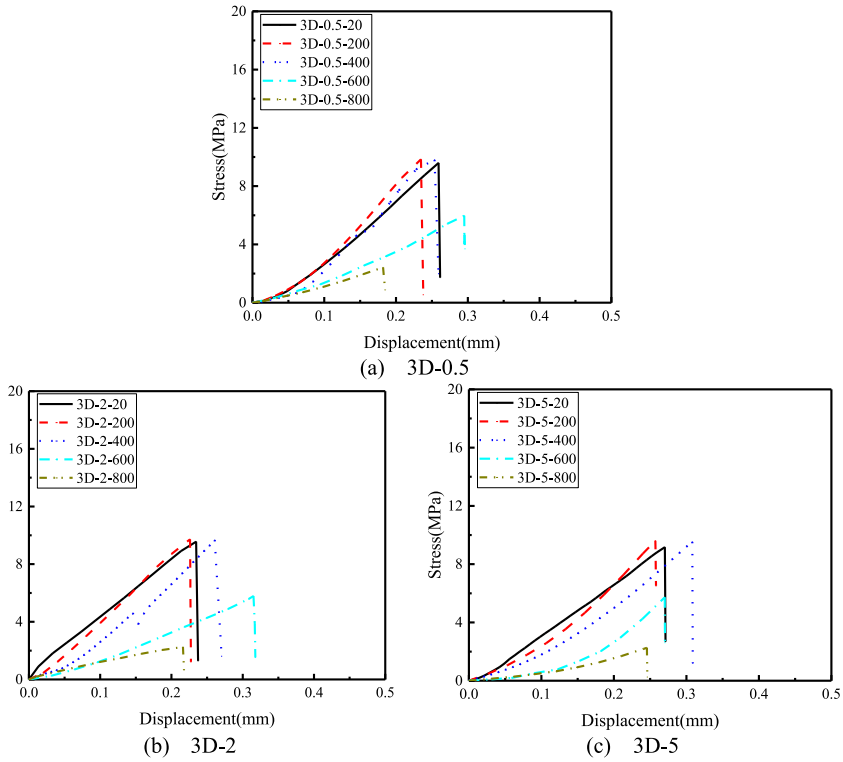

Fig. 9. 3DP-UHPC bond stress-strain relationship curve.

bonding post-elevated temperatures not only enriches our understanding of this material but also provides actionable guidance for its implementation in construction. These results can inform the development of new standards for 3DP-UHPC structures, contributing to the creation of more resilient built environments.

3.3. Experimental results and analysis of bonding performance of 3DP-UHPC after elevated temperature

3.3.1. Test results of bonding performance of 3DP-UHPC after elevated temperature

The bond stress-strain curves of 3DP-UHPC and MC-UHPC hybrid fibres with different interlayer time intervals after different temperatures are shown in Figs. 9 and 10. When the specimen reached the peak stress of adhesive tension σ_p, regardless of the target temperature, time interval, and preparation method, the stress exhibited a sharp decrease, and the specimen underwent brittle failure under tensile action. This brittle failure was due to the lack of fibre connections at the interlayer bonding strip of 3DP-UHPC to provide ductility, resulting in brittle failure. MC-UHPC simulated the interface situation of 3DP-UHPC, and there were no fibre connections between the bonding strips, which also resulted in brittle failure. Fig. 11 shows the cross section of 3DP-UHPC and MC-UHPC.

Strain gauges were applied to the specimens to measure their tensile strain, and the resulting data was used to generate bond stress-strain curves (Fig. 12, Fig. 13). However, these curves did not exhibit a descending segment for any of the specimens. This is because the strain gauge fails once the specimen cracks, rendering it impossible to record the tensile strain beyond that point. Therefore, the stress-strain curves in Figs. 12 and 13 represented the behaviour of the specimens before cracking occurred. The maximum strain

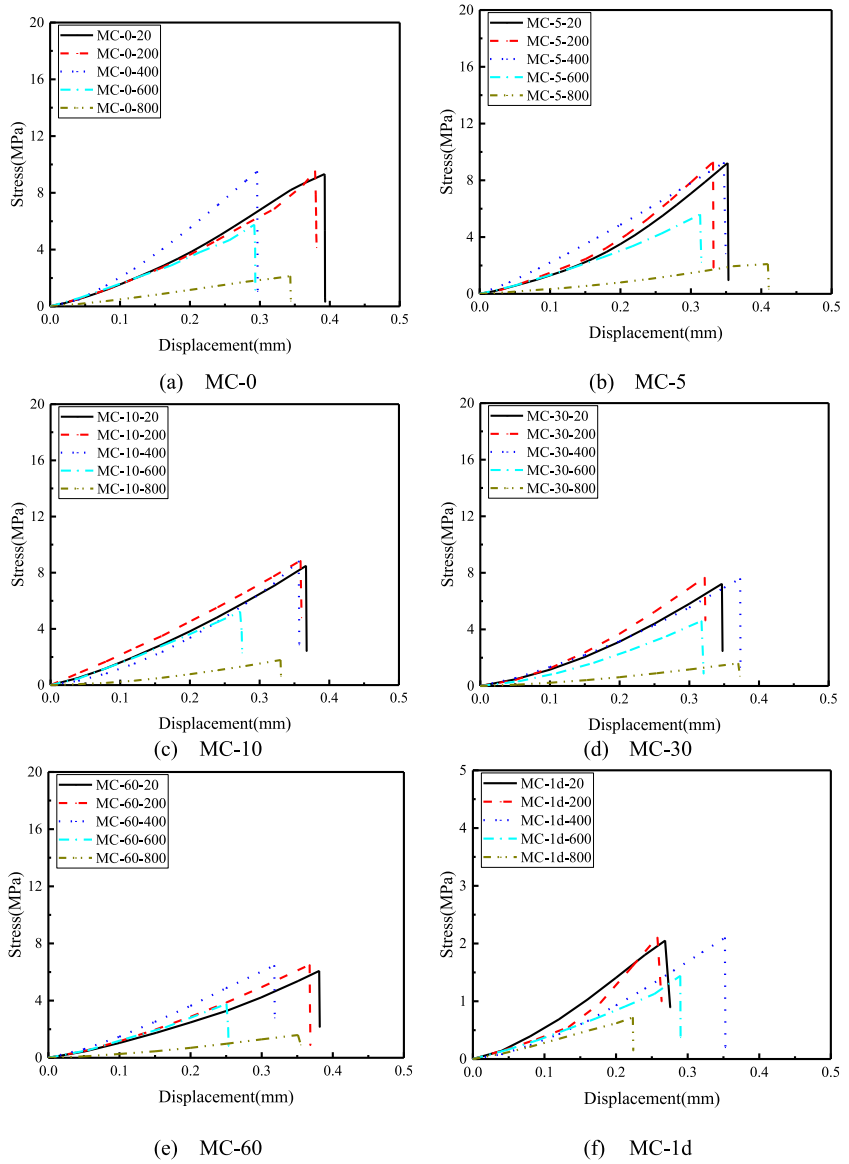

Fig. 10. MC-UHPC bond stress-strain relationship curve.

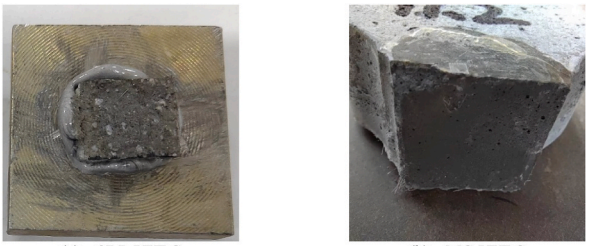

(a) 3DP-UHPC (b) MC-UHPC

Fig. 11. Cross section of 3DP-UHPC and MC-UHPC.

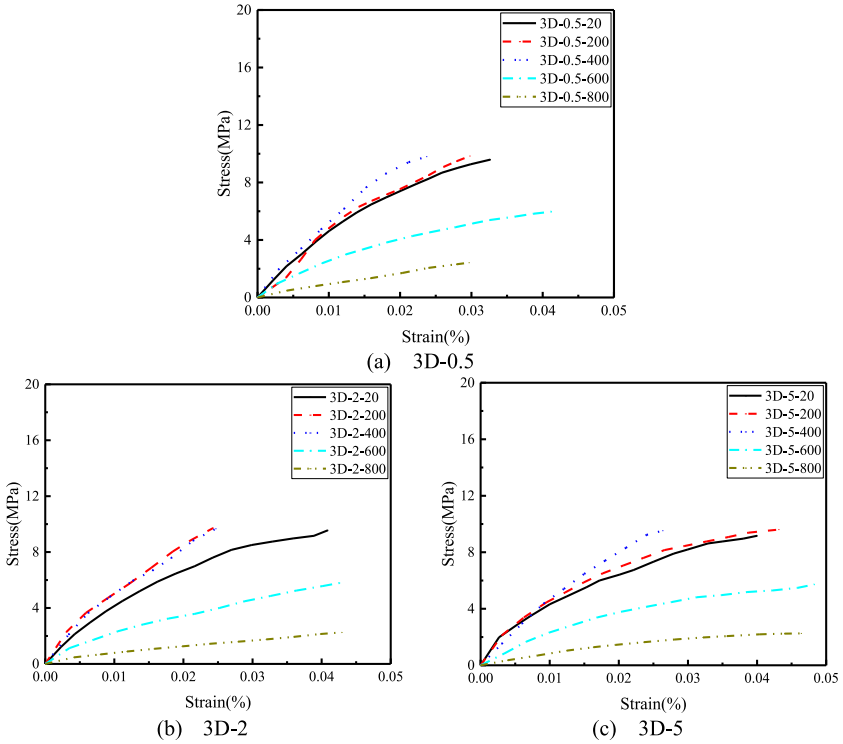

Fig. 12. 3DP-UHPC bond stress-strain curve.

recorded by the strain gauge corresponded to the cracking strain ε_{ck}, while the corresponding stress represented the cracking stress σ_{ck}. Table 9 and Table 10 provide the bonding tensile mechanical parameters for 3DP-UHPC and MC-UHPC, respectively. When the specimens cracked, they underwent immediate brittle failure. Hence, the bonding tensile stress that each specimen borne at the point of cracking was the maximum stress it could withstand, which was equal to σ_{ck} and σ_p. At the given target temperature, the maximum strain σ_p observed in 3DP-UHPC reached 9.84 MPa. Additionally, the peak strain ε_p for all specimens failed within the range of 0.023–0.049 %. This indicated that the specimens were prone to cracking even under small amounts of tensile deformation.

The bond tensile failure modes of 3DP-UHPC and MC-UHPC specimens could be observed in Fig. 14 and Fig. 15. Owing to the cracking of all specimens at the intermediate bonding strip, the bond tensile test data obtained in this experiment was reliable. At the bonding strip, there was no steel fibre connection between concrete and mortar, they were only connected by bonding force. When the load exceeded the tensile strength of concrete, the specimen would fail from the bonding strip without fibre connections.

3.3.2. Bonding strength of 3DP-UHPC after elevated temperature

Fig. 16 illustrates the change in bonding strength between 3DP-UHPC and MC-UHPC as a function of the target temperature. With increasing target temperature, both 3DP-UHPC and MC-UHPC exhibited an initial increase followed by a decrease in bonding strength. At 200 °C, the positive effects described in section 3.2 were fully manifested. The hydration products resulting from cement hydration and volcanic ash reactions effectively filled the voids in the bonding strip, leading to improved macroscopic bonding strength. During heating at 400 °C, the polypropylene fibres underwent melting and volatilization, which created interconnected pores in conjunction with existing free water and capillary water pores, forming a connected pore structure. The elevated-temperature environment could cause damage to this pore structure, ultimately impacting the strength of the concrete [43]. Thus, at 400 °C, the bonding strength of

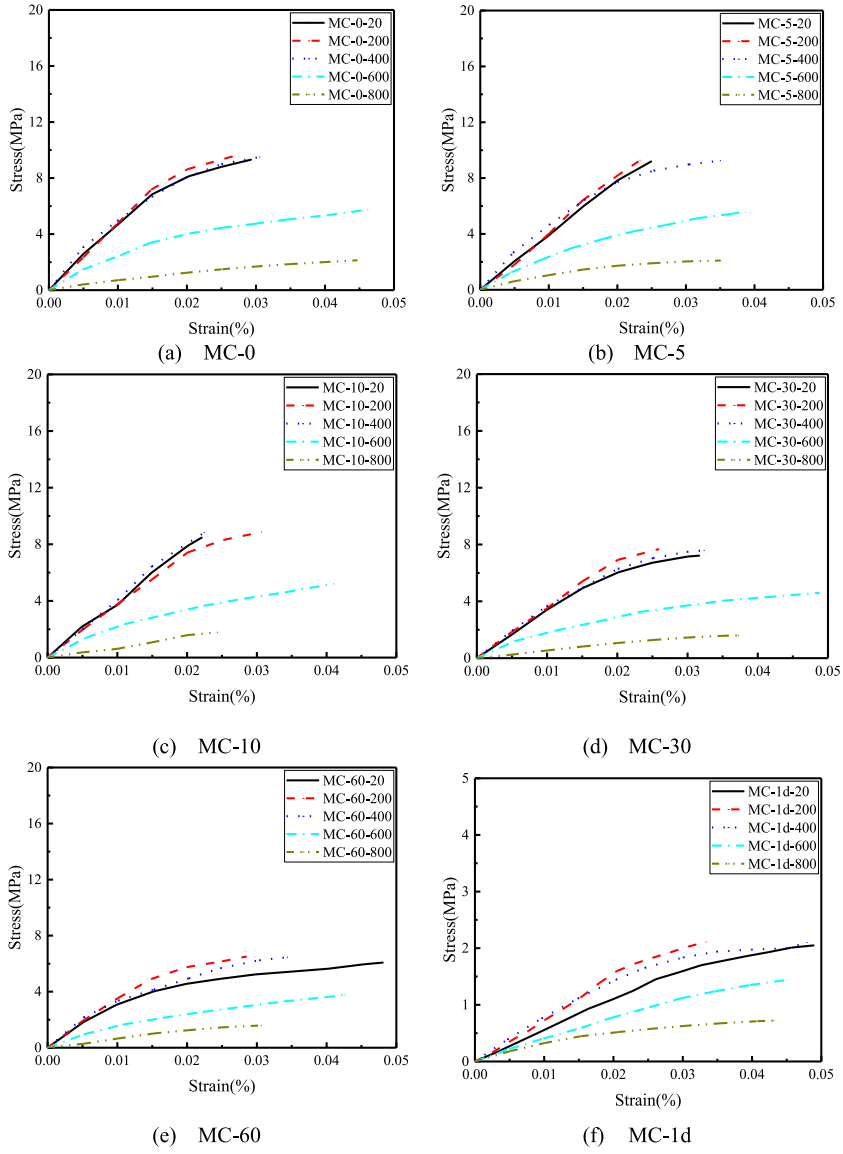

Fig. 13. MC-UHPC bond stress-strain curve.

both 3DP-UHPC and MC-UHPC might slightly decrease as compared to 200 °C due to the damage caused by the volatilization of polypropylene fibres. However, if the target temperature was lower than the evaporation temperature of polypropylene fibres, the damage to the concrete pores caused by elevated temperature would be minimized. Thus, the potential improvement and attainment of the maximum bonding strength depend on specific conditions, necessitating further investigation to understand the changes in bonding strength of 3DP-UHPC under different temperature conditions. This research would offer enhanced insights into the influence of elevated temperatures on the structural performance of 3DP-UHPC. After exposure to temperatures of 600 °C and 800 °C, both 3DP-UHPC and MC-UHPC exhibited loose and porous bonding strips. Some specimens even exhibited complete failure of the bonding joints, leading to a sharp decline in bonding strength. The bonding strength at these elevated temperatures decreased to approximately 60 % and 20 % of the bonding strength observed after 400 °C, respectively.

Fig. 17 shows the changes in bond strength of various types of 3DP-UHPC and MC-UHPC at different interlayer time intervals. Fig. 17(a) shows the variation in 3DP-UHPC bonding strength with interlayer time intervals at various target temperatures. As the interlayer time interval increased, the overall bonding strength of 3DP-UHPC specimens after different temperatures exhibited a decreasing trend. During the interlayer time interval from 0.5 min to 5 min, the bonding strength of specimens at each target temperature (20 °C, 200 °C, 400 °C, 600 °C, and 800 °C) decreased by 4.38 %, 2.34 %, 2.76 %, 4.02 %, and 6.61 %. Compared with 20 °C, the loss rate of bonding strength of the specimen after 200 °C treatment has declined, which might be attributed to the further hydration process reducing the difference in bonding performance caused by interlayer time intervals to some extent. As the hydration reaction progressed, the hydration products in the cement matrix would continuously form and increase, filling the pores of the

Table 9
3DP-UHPC bond performance parameters.

		Temperature (°C)				
		20	200	400	600	800
3D-0.5	σ_p (MPa)	9.59	9.84	9.80	5.97	2.42
	σ_{ck} (MPa)	9.59	9.84	9.80	5.97	2.42
	Standard deviation	0.08	0.34	0.42	1.02	0.12
	ε_{ck} (%)	0.033	0.030	0.024	0.041	0.030
	Elastic modulus (GPa)	45.92	47.93	47.70	24.20	8.69
3D-2	σ_p (MPa)	9.56	9.72	9.67	5.79	2.25
	σ_{ck} (MPa)	9.56	9.72	9.67	5.79	2.25
	Standard deviation	0.71	0.36	0.14	0.44	0.42
	ε_{ck} (%)	0.041	0.024	0.025	0.042	0.043
	Elastic modulus (GPa)	39.57	50.84	50.19	15.52	6.67
3D-5	σ_p (MPa)	9.17	9.61	9.53	5.75	2.26
	σ_{ck} (MPa)	9.17	9.61	9.53	5.75	2.26
	Standard deviation	0.43	0.08	0.32	0.82	0.48
	ε_{ck} (%)	0.040	0.043	0.026	0.048	0.046
	Elastic modulus (GPa)	41.33	44.97	43.71	21.31	8.12

Table 10
MC-UHPC bond performance parameters.

		Temperature (°C)				
		20	200	400	600	800
MC-0	σ_p (MPa)	9.32	9.55	9.50	5.73	2.13
	σ_{ck} (MPa)	9.32	9.55	9.50	5.73	2.13
	Standard deviation	1.05	0.38	0.46	0.65	0.28
	ε_{ck} (%)	0.029	0.027	0.031	0.046	0.044
	Elastic modulus (GPa)	46.93	47.83	50.19	23.01	6.28
MC-5	σ_p (MPa)	9.21	9.28	9.25	5.59	2.10
	σ_{ck} (MPa)	9.21	9.28	9.25	5.59	2.10
	Standard deviation	0.35	0.12	0.44	0.98	0.08
	ε_{ck} (%)	0.025	0.023	0.043	0.039	0.035
	Elastic modulus (GPa)	40.09	44.55	44.24	22.45	10.47
MC-10	σ_p (MPa)	8.49	8.86	8.83	5.22	1.78
	σ_{ck} (MPa)	8.49	8.86	8.83	5.22	1.78
	Standard deviation	0.07	0.44	0.48	0.068	0.26
	ε_{ck} (%)	0.022	0.031	0.023	0.041	0.024
	Elastic modulus (GPa)	37.34	39.84	39.18	21.41	6.83
MC-30	σ_p (MPa)	7.22	7.68	7.59	4.60	1.60
	σ_{ck} (MPa)	7.22	7.68	7.59	4.60	1.60
	Standard deviation	0.47	1.12	0.68	0.34	0.41
	ε_{ck} (%)	0.032	0.026	0.037	0.048	0.037
	Elastic modulus (GPa)	33.94	35.39	35.37	17.28	5.47
MC-60	σ_p (MPa)	6.08	6.51	6.46	3.77	1.59
	σ_{ck} (MPa)	6.08	6.51	6.46	3.77	1.59
	Standard deviation	0.71	0.32	0.29	0.66	0.12
	ε_{ck} (%)	0.048	0.029	0.036	0.042	0.031
	Elastic modulus (GPa)	31.70	33.23	33.00	15.31	6.90
MC-1d	σ_p (MPa)	2.05	2.11	2.10	1.44	0.72
	σ_{ck} (MPa)	2.05	2.11	2.10	1.44	0.72
	Standard deviation	0.13	0.37	0.08	0.34	0.16
	ε_{ck} (%)	0.049	0.033	0.048	0.045	0.043
	Elastic modulus (GPa)	5.68	7.30	7.66	3.91	3.12

bonding strip, and improving the density and internal structure of the material. This could improve the quality of interlayer bonding and reduce the negative impact of time intervals on bonding performance. However, within the target temperature range of 200–800 °C, the bonding strength loss of 3DP-UHPC with an interlayer time interval of 5 min gradually increased as compared to 3DP-UHPC with an interlayer time interval of 0.5 min. This might be due to elevated temperature heating causing stress inside the specimen and causing dimensional changes. Owing to the different initial states of specimens at different time intervals, the differences in thermal expansion and contraction during the heating and cooling processes might further amplify the differences in bonding performance. This is consistent with the analysis in section 3.2.2.

Fig. 17(b) illustrates the variation in bonding strength of MC-UHPC specimens with interlayer time intervals at different target temperatures. The results indicated that as the interlayer time interval increased, the bonding strength gradually decreased. For shorter time intervals (such as 0–10 min), the specimens exhibited higher bonding strength after 20 °C and 200 °C. This could be attributed to

Fig. 14. 3DP-UHPC bond tensile failure mode.

the fact that specimens poured within a shorter time period could form a finer and denser structure, which promoted better bonding. However, after 600 °C and 800 °C, the bonding strength significantly decreased. This could be due to accelerated thermal expansion and contraction, as well as damage to the pores of the bonding strip, leading to a decline in bonding strength. For longer time intervals, the specimens exhibited lower bonding strength across the temperature range of 20 °C–800 °C. This might be a result of significant differences in shrinkage, settlement, and other factors between fresh and aged concrete caused by longer time intervals. The secondary hydration reaction of cement before 400 °C did not mitigate the negative impact of time intervals on bonding strength. However, after reaching 400 °C, the damage caused by elevated temperatures intensified the negative impact, resulting in a bonding strength of only 0.72 MPa for the MC-1d-800 specimen.

Fig. 18 shows the comparison of bonding strength between 3DP-UHPC and MC-0 and MC-5 at various target temperatures. Except for 3D-5-20 and 3D-5-400, the bonding strength of all types of 3DP-UHPC was greater than that of MC-UHPC with similar interlayer time intervals at the same target temperature. The bonding strength of 3DP-UHPC was observed to be higher due to the compaction effect of the 3D printing process nozzle. This finding aligns with the analysis results of the bonding strip's microstructure discussed in section 3.2.

This section's findings on the bonding strength trends of 3DP-UHPC at elevated temperatures are key for material selection and design in thermally stressed construction environments. While the results provide guidance for enhancing structural safety, the study has limitations, including a controlled experimental setup that did not account for all real-world conditions and a limited temperature range. The use of specific fibres and mixes may not be generalizable to all applications, and long-term durability aspects require further investigation.

In light of these limitations, future research should be expanded on the temperature range, incorporation of multi-factorial environmental effects, and exploration of long-term durability of 3DP-UHPC. Advanced 3D printing techniques to improve inter-layer bonding and durability are also recommended.

In summary, the analysis advances our understanding of 3DP-UHPC behaviour under elevated temperatures and sets the stage for developing more resilient structures, while highlighting areas for further study.

3.4. Establishment of a relationship model for interface bonding performance of 3DP-UHPC after elevated temperature

To characterize the interfacial bonding behaviour of hybrid fibre 3DP-UHPC after elevated temperatures and provide more

Fig. 15. MC-UHPC bond tensile failure mode.

theoretical basis for the elevated-temperature resistant analysis of 3D printed buildings, a model suitable for the interface bonding strength relationship of hybrid fibre 3DP-UHPC after elevated temperatures was established.

In this experiment, due to limitations in the size of the equipment, the interlayer time interval of 3DP-UHPC was relatively short. However, in practical large-scale on-site 3D printing construction processes, the time intervals between each layer might be extended. Through the MC-UHPC experiment simulating the interlayer situation of 3DP-UHPC, it was observed that both MC-UHPC and 3DP-UHPC exhibited similar failure modes, that was, failure occurred from the bonding strip without fibre connections. In addition, there was a similar stress-strain relationship curve between MC-UHPC and 3DP-UHPC. Therefore, it was believed that the interlayer bonding performance of MC-UHPC could approximately represent the interlayer bonding performance of 3DP-UHPC. To validate this hypothesis and characterize the interfacial bonding behaviour of 3DP-UHPC following exposure to elevated temperatures, it was necessary to establish a rational model using experimental data from MC-UHPC and calculate the interlayer strength. This model could then be applied to predict and analyse the bonding behaviour of 3DP-UHPC.

Drawing upon the dynamic tensile stress-strain curve fitting as delineated by the Zhu-Wang-Tang (ZWT) constitutive model, as

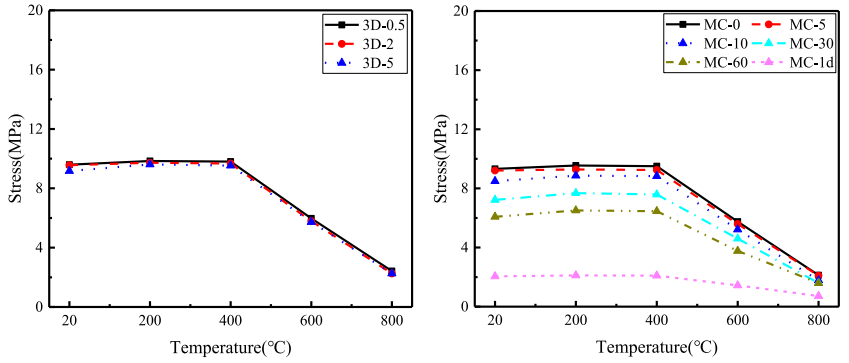

(a) The variation in 3DP-UHPC bonding strength with temperature

(b) The variation in MC-UHPC bonding strength with temperature

Fig. 16. Comparison of bonding strength of various specimen types after different temperatures.

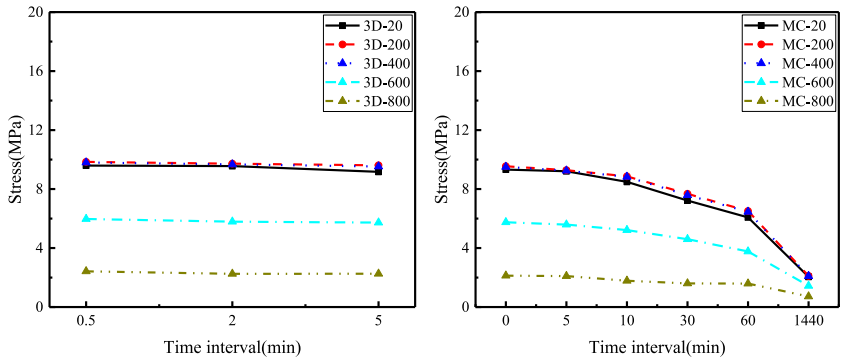

(a) The variation in 3DP-UHPC bonding strength with interlayer time interval

(b) The variation in MC-UHPC bonding strength with interlayer time interval

Fig. 17. Comparison of bonding strength varied among different types of specimens with different interlayer time intervals.

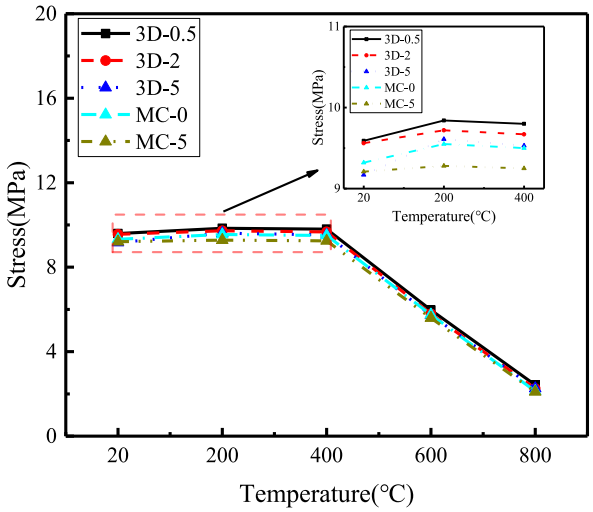

Fig. 18. Comparison of bonding strength of specimens with different pouring methods.

proposed by Zhang et al. [64], and taking into account that the bond stress-strain curve derived from the current experiment encompasses solely the elastic stage (Stage I) and the hardening stage (Stage II), a constitutive model for the interface bonding performance of 3DP-UHPC after elevated temperatures is proposed. The model is represented in Fig. 19, culminating in the formulation of an interface bonding constitutive model (Eq. (1)) for 3DP-UHPC after elevated temperatures:

$$\sigma = \begin{cases} E_{tt,y(TI)}\varepsilon & \varepsilon \le \varepsilon_{tt,y(TI)} \\ \sigma_{tt,y(TI)} + \left(\sigma_{pt,y(TI)}\text{-}\sigma_{tt,y(TI)}\right)\dfrac{r\left[\left(\varepsilon\text{-}\varepsilon_{tt,y(TI)}\right)/\left(\varepsilon_{pt,y(TI)}\text{-}\varepsilon_{tt,y(TI)}\right)\right]}{r\text{-}1+\left[\left(\varepsilon\text{-}\varepsilon_{tt,y(TI)}\right)/\left(\varepsilon_{pt,y(TI)}\text{-}\varepsilon_{tt,y(TI)}\right)\right]^r} & \varepsilon_{tt,y(TI)} < \varepsilon \le \varepsilon_{pt,y(TI)} \end{cases} \quad (1)$$

where, t represents the temperature (°C); $y(TI)$ is a function of time interval TI; $E_{tt,y(TI)}$ is the interface bonding elastic modulus of 3DP-UHPC with t and $y(TI)$ as independent variables; $\sigma_{tt,y(TI)}$ is the maximum bonding stress of elastic stage of 3DP-UHPC with t and $y(TI)$ as independent variables; $\varepsilon_{tt,y(TI)}$ is the maximum bonding strain of elastic stage of 3DP-UHPC with t and $y(TI)$ as independent variables; $\sigma_{pt,y(TI)}$ is the peak bonding stress of 3DP-UHPC with t and $y(TI)$ as independent variables; $\varepsilon_{pt,y(TI)}$ is the peak bonding strain of 3DP-UHPC with t and $y(TI)$ as independent variables; $r = \frac{E_{tt,y(TI)}}{E_{tt,y(TI)}-E_{pt,y(TI)}}$, $E_{pt,y(TI)} = \frac{\sigma_{pt,y(TI)}-\sigma_{tt,y(TI)}}{\varepsilon_{pt,y(TI)}-\varepsilon_{tt,y(TI)}}$. Referring to the provisions of National Standard GB 50010–2010 [65] that the specimen entered the hardening stage when the strain reached $0.5\sigma_{pt,y(TI)}$.

Firstly, fit $y(TI)$ with TI as a function, and the fitting results are illustrated in Fig. 20. The functional relationship is shown in Eq. (2):

$$y(TI) = 0.97 + 1.62\left(1\text{-}e^{\text{-}TI/6.69}\right) + 3.42\left(1\text{-}e^{\text{-}TI/50.93}\right) \quad (2)$$

The coefficient of determination $R^2 = 0.983$ indicated that Eq. (2) could better represent the conversion relationship between $y(TI)$ and TI.

Then, based on the test data of MC-UHPC, nonlinear surface fittings were performed on $E_{tt,y(TI)}$, $\varepsilon_{pt,y(TI)}$ and $\sigma_{pt,y(TI)}$ with respect to t and $y(TI)$, as shown in Fig. 21. The final model formula obtained are presented in Eqs. (3)–(5):

$$E_{tt,y(TI)} = 49.03 + (1.81\text{E-}3)t + 0.84y(TI)\text{-}(7.95\text{E-}5)t^2\text{-}1.29y(TI)^2 + (7.85\text{E-}3)ty(TI) \quad (3)$$

$$\varepsilon_{pt,y(TI)} = 0.04\text{-}(9.03\text{E-}5)t\text{-}0.01y(TI)\text{-}(8.73\text{E-}6)ty(TI) + (4.09\text{E-}7)t^2 + (3.61\text{E-}3)y(TI)^2\text{-}(3.33\text{E-}10)t^3\text{-}(2.33\text{E-}4)y(TI)^3 + (4.20\text{E-}7)ty(TI)^2 \quad (4)$$

$$\sigma_{pt,y(TI)} = 7.65 + (6.26\text{E-}3)t + 1.09y(TI)\text{-}(1.63\text{E-}5)t^2\text{-}0.30y(TI)^2 \quad (5)$$

The nonlinear fitting results between the temperature, time interval, and $E_{tt,y(TI)}$, $\varepsilon_{pt,y(TI)}$, $\sigma_{pt,y(TI)}$ of MC-UHPC were good. By substituting Eqs. (2)–(5) into Eq. (1), the constitutive formula applicable to this model was derived, and the calculation results are shown in Fig. 22.

The stress–strain curves calculated by the constitutive model proposed in this study fitted well with the test results of 3DP-UHPC. This indicated that the proposed interface bonding strength relationship model after elevated temperature could be applied to 3DP-UHPC.

However, it should be pointed out that although a certain degree of consistency was achieved during the validation process, it does not fully guarantee the universal reliability of the relational model under different conditions. In order to fully validate the reliability of the relationship model, it is necessary to consider more factors and conduct more experiments. For example, using different types of 3DP-UHPC materials, dealing with different interlayer time intervals, and simulating different elevated-temperature environments. In addition, the predictions established by the relational model are still based on observed phenomena and experimental data, which may have some errors. Therefore, in practical applications, judgments and decisions should be made based on the actual situation.

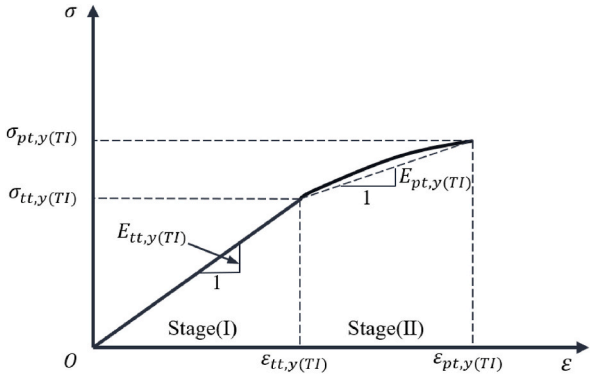

Fig. 19. The constitutive model.

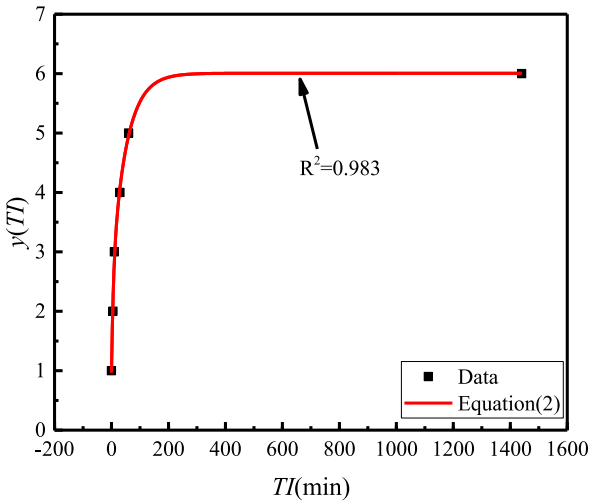

Fig. 20. Function fitting results of $y(TI)$ and TI

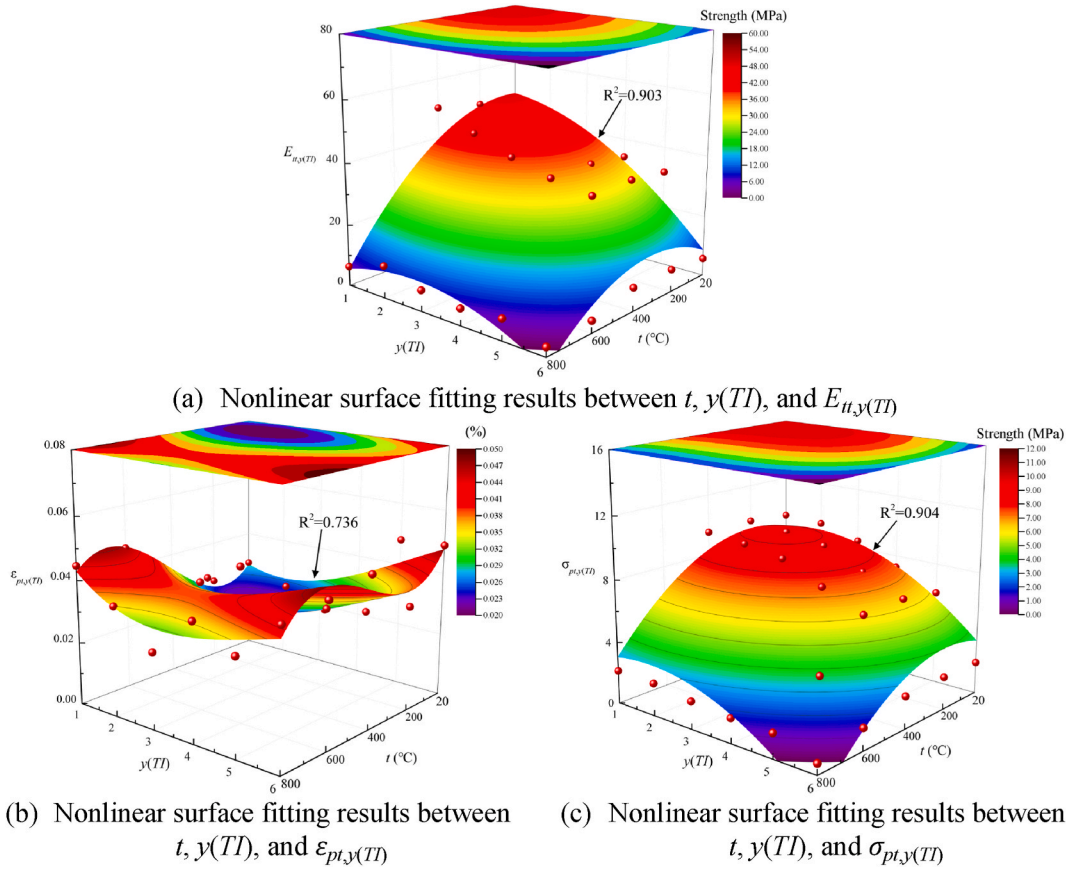

(a) Nonlinear surface fitting results between t, $y(TI)$, and $E_{tt,y(TI)}$

(b) Nonlinear surface fitting results between t, $y(TI)$, and $\varepsilon_{pt,y(TI)}$

(c) Nonlinear surface fitting results between t, $y(TI)$, and $\sigma_{pt,y(TI)}$

Fig. 21. Nonlinear surface fitting results.

4. Conclusion

This study investigated the microstructure and bonding characteristics of hybrid fibre 3DP-UHPC with different interlayer time intervals after exposure to various temperatures, using MC-UHPC with different pouring time intervals as a control group to explore the differences in bonding performance between 3D printed and mould-casting concrete. The findings of this research lead to the following conclusions.

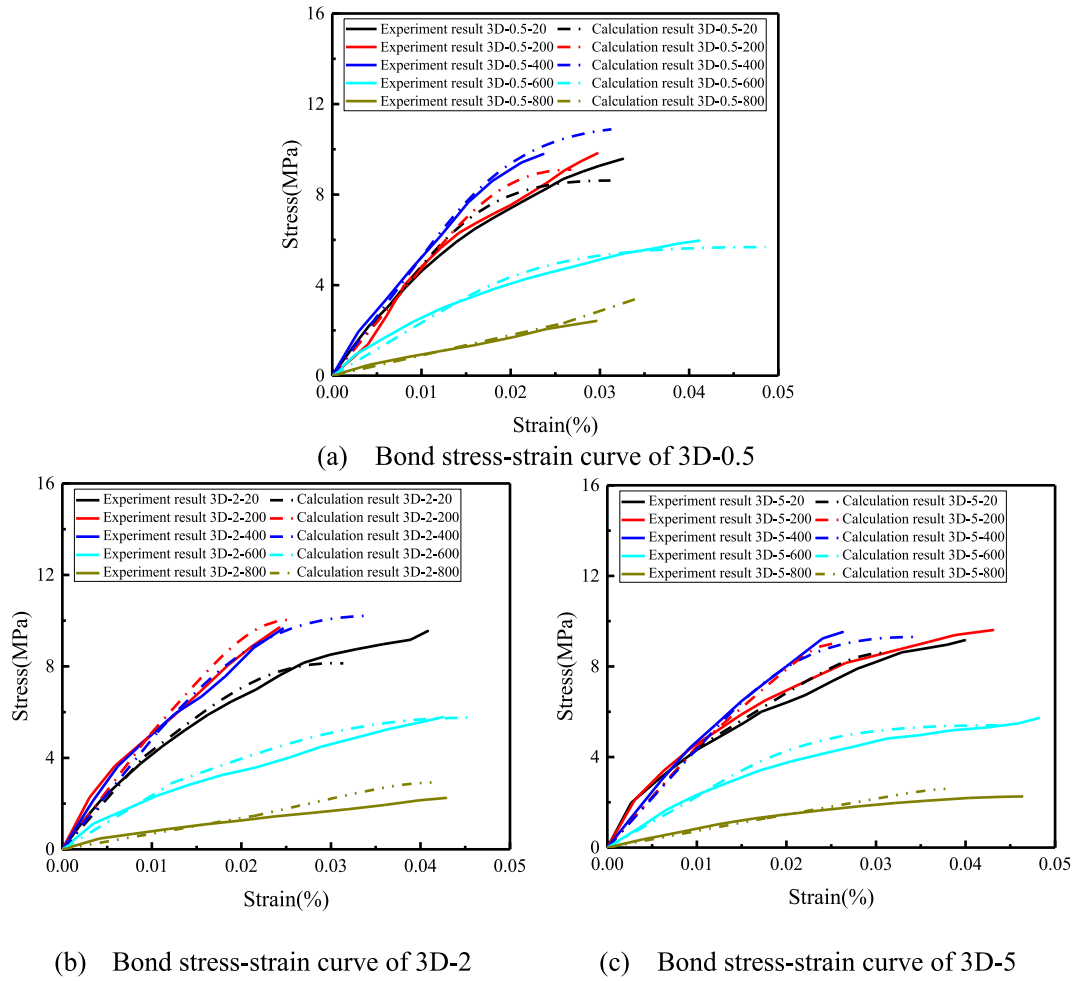

Fig. 22. Comparison between predicted and experimental results.

1. Some specimens experienced local damage when subjected to 800 °C. The incorporation of polypropylene fibres improved the elevated-temperature stability of the hybrid fibre 3DP-UHPC specimens, suggesting potential benefits in environments prone to elevated temperatures or fires.
2. Both MC-UHPC and 3DP-UHPC failed at the bonding strip after elevated temperature exposure. The lack of steel fibre connections at the bonding strip, which relied solely on bonding force to unite concrete and mortar, was identified as the critical point of failure when tensile loads exceeded the concrete's strength.
3. At 400 °C, the melting and evaporation of polypropylene fibres led to the formation of a connected pore structure, which slightly reduced the interface bonding strength of 3DP-UHPC as compared to that at 200 °C. Further exposure to 600 °C and 800 °C resulted in loose and porous bonding strips for both 3DP-UHPC and MC-UHPC, causing a significant decline in bonding strength.
4. An increase in the interlayer time interval was associated with a gradual decrease in bonding strength, likely due to differences in shrinkage, settlement, and other factors between fresh and aged concrete. This highlights the importance of precise construction scheduling to ensure optimal bonding and structural integrity.
5. The interface bonding strength relationship model proposed in this study could be applied to hybrid fibre 3DP-UHPC after elevated temperature.

The study's findings offer critical insights for the construction industry, highlighting the impact of temperature and interlayer timing on 3DP-UHPC bonding, essential for structures in harsh climates or fire-prone areas. The results encourage advancements in 3D printing to enhance component durability and structural resilience.

Future research directions

Building upon these findings, future research should focus on the long-term durability of 3DP-UHPC under sustained elevated temperatures and the development of innovative 3D printing techniques to further enhance interlayer bonding. Additionally, the exploration of alternative fibre types and their effects on elevated-temperature performance could provide valuable insights for the

development of more resilient 3DP-UHPC formulations. The implementation of monitoring technologies within 3DP-UHPC structures to track their performance over time is also recommended.

In conclusion, this research enhances the understanding of 3DP-UHPC performance after elevated temperatures and provides actionable guidance for its use in building more robust and enduring infrastructure. The suggestions for future research presented here aim to build upon these findings and continue to advance the field of 3D printed construction materials.

CRediT authorship contribution statement

Liang Dong: Conceptualization, Methodology, Investigation, Data Curation, Writing – original draft, Writing – review & editing. **Yekai Yang:** Conceptualization, Methodology, Writing – review & editing, Visualization, Supervision. **Zhongxian Liu:** Resources, Investigation, Software, Project administration. **Yan Zhang:** Resources, Data Curation. **Chengqing Wu:** Conceptualization, Methodology, Writing – review & editing, Visualization, Supervision.

Declaration of competing interest

We wish to confirm that there are no known conflicts of interest associated with this publication and there has been no significant financial support for this work that could have influenced its outcome.

We confirm that the manuscript has been read and approved by all named authors and that there are no other persons who satisfied the criteria for authorship but are not listed. We further confirm that the order of authors listed in the manuscript has been approved by all of us.

We confirm that we have given due consideration to the protection of intellectual property associated with this work and that there are no impediments to publication, including the timing of publication, with respect to intellectual property. In doing so we confirm that we have followed the regulations of our institutions concerning intellectual property.

We understand that the Corresponding Author is the sole contact for the Editorial process (including Editorial Manager and direct communications with the office). He is responsible for communicating with the other authors about progress, submissions of revisions and final approval of proofs. We confirm that we have provided a current, correct email address which is accessible by the Corresponding Author and which has been configured to accept email from Chengqing.wu@uts.edu.au.

Data availability

Data will be made available on request.

Acknowledgement

The research presented herein is supported by the National Natural Science Foundation of China (Grant No.51978186), the Science and Technology Project of Hebei Education Department (Grant No. QN2023190).

References

[1] L. Wang, H. Ma, Z. Li, G. Ma, J. Guan, Cementitious composites blending with high belite sulfoaluminate and medium-heat Portland cements for largescale 3D printing, Addit. Manuf. 46 (2021) 102189.
[2] B. Bhushan, M. Caspers, An overview of additive manufacturing (3D printing) for microfabrication, Microsyst. Technol. 23 (2017) 1117–1124.
[3] J. Norman, R.D. Madurawe, C.M. Moore, M.A. Khan, A. Khairuzzaman, A new chapter in pharmaceutical manufacturing: 3D-printed drug products, Adv. Drug Deliv. Rev. 108 (2017) 39–50.
[4] J. Xiao, G. Ji, Y. Zhang, G. Ma, V. Mechtcherine, J. Pan, S. Du, Large-scale 3D printing concrete technology: current status and future opportunities, Cement Concr. Compos. 122 (2021) 104115.
[5] R.A. Buswell, W.L. De Silva, S.Z. Jones, J. Dirrenberger, 3D printing using concrete extrusion: a roadmap for research, Cement Concr. Res. 112 (2018) 37–49.
[6] G. Ma, J. Sun, L. Wang, F. Aslani, M. Liu, Electromagnetic and microwave absorbing properties of cementitious composite for 3D printing containing waste copper solids, Cement Concr. Compos. 94 (2018) 215–225.
[7] T.T. Le, S.A. Austin, S. Lim, R.A. Buswell, A.G. Gibb, T. Thorpe, Mix design and fresh properties for high-performance printing concrete, Mater. Struct. 45 (2012) 1221–1232.
[8] I. Agustí-Juan, F. Müller, N. Hack, T. Wangler, G. Habert, Potential benefits of digital fabrication for complex structures: environmental assessment of a robotically fabricated concrete wall, J. Clean. Prod. 154 (2017) 330–340.
[9] E.C. Vergara, B.L. Aguirregabiria, J.M.L. Pérez, G.O. Vacarezza, Innovative free-form glass fiber reinforced concrete (GRC) panel, Revista de la Construccion 16 (3) (2017) 479–488.
[10] I. Agustí-Juan, G. Habert, Environmental design guidelines for digital fabrication, J. Clean. Prod. 142 (2017) 2780–2791.
[11] D.Y. Yoo, H.O. Shin, J.Y. Lee, Y.S. Yoon, Enhancing cracking resistance of ultra-high-performance concrete slabs using steel fibres, Mag. Concr. Res. 67 (10) (2015) 487–495.
[12] Y. Yang, C. Wu, Z. Liu, Y. Qin, W. Wang, Comparative study on square and rectangular UHPFRC-Filled steel tubular (CFST) columns under axial compression, Structures 34 (2021) 2054–2068.
[13] P. Wu, C. Wu, Z. Liu, S. Xu, J. Li, J. Li, Triaxial strength and failure criterion of ultra-high performance concrete, Adv. Struct. Eng. 25 (9) (2022) 1893–1906.
[14] L. Dong, Y. Yang, Z. Liu, T. Yang, C. Xue, R. Shao, C. Wu, Effect of chloride ion migration behaviour on the microstructure and mechanical properties of ultra-high performance concrete: a review, J. Build. Eng. 82 (9) (2023) 108233.
[15] Y. Zhang, X. Li, Y. Zhu, X. Shao, Experimental study on flexural behavior of damaged reinforced concrete (RC) beam strengthened by toughness-improved ultra-high performance concrete (UHPC) layer, Compos. B Eng. 186 (2020) 107834.
[16] M. Zhou, W. Lu, J. Song, G.C. Lee, Application of ultra-high performance concrete in bridge engineering, Construct. Build. Mater. 186 (2018) 1256–1267.
[17] Y. Yang, C. Wu, Z. Liu, H. Wang, Q. Ren, Mechanical anisotropy of ultra-high performance fibre-reinforced concrete for 3D printing, Cement Concr. Compos. 125 (2022) 104310.
[18] Y. Yang, C. Wu, Z. Liu, H. Zhang, 3D-printing ultra-high performance fiber-reinforced concrete under triaxial confining loads, Addit. Manuf. 50 (2022) 102568.

[19] A.R. Arunothayan, B. Nematollahi, R. Ranade, J.G. Sanjayan, K.H. Khayat, Fiber orientation effects on ultra-high performance concrete formed by 3D printing, Cement Concr. Res. 143 (2021) 106384.
[20] G. Bai, L. Wang, F. Wang, X. Cheng, Investigation of the printability and mechanical properties of 3D printing UHPC, Materials Reports 35 (12) (2021) 67–73.
[21] Z. Sun, Y. Sun, M. Pang, Y. Zhao, Y. Xu, H. Li, Y. Xu, Preparation of ultra high performance concrete for 3D printing construction, New Building Materials 48 (1) (2021) 1–5.
[22] Y. Yang, C. Wu, Z. Liu, J. Li, T. Yang, X. Jiang, Characteristics of 3D-printing ultra-high performance fibre-reinforced concrete under impact loading, Int. J. Impact Eng. 164 (2022) 104205.
[23] Y. Yang, C. Wu, Z. Liu, Rate dependent behaviour of 3D printed ultra-high performance fibre-reinforced concrete under dynamic splitting tensile, Compos. Struct. 309 (2023) 116727.
[24] G. Ma, G. Bai, L. Wang, F. Wang, Explosion resistance of 3D printing ultra-high performance concrete based on contact explosion tests, Int. J. Impact Eng. 169 (2022) 104316.
[25] Y. Zhao, Preparation and Performance Research of Ultra High Performance Concrete Based on 3D Printing, Shandong Jianzhu University, 2023.
[26] G. Bai, L. Wang, F. Wang, G. Ma, In-process reinforcing method: dual 3D printing procedure for ultra-high performance concrete reinforced cementitious composites, Mater. Lett. 304 (2021) 130594.
[27] Y.S. Tai, H.H. Pan, Y.N. Kung, Mechanical properties of steel fiber reinforced reactive powder concrete following exposure to high temperature reaching 800 C, Nucl. Eng. Des. 241 (7) (2011) 2416–2424.
[28] B. Luo, Study on Explosive Spalling Rules and Mechanical Properties of Reactive Powder Concrete at Elevated Temperatures, Harbin Institute of Technology, 2014.
[29] Y. Kang, Experimental Study on Residual Mechanical Properties of Reactive Powder Concrete with Hybrid Fibers after Exposure to High Temperature, Beijing Jiaotong University, 2011.
[30] H.S. So, H.S. Jang, J. Khulgadai, S.Y. So, Mechanical properties and microstructure of reactive powder concrete using ternary pozzolanic materials at elevated temperature, KSCE J. Civ. Eng. 19 (2015) 1050–1057.
[31] L. Dong, Y. Yang, Z. Liu, Q. Ren, J. Li, Y. Zhang, C. Wu, Microstructure and mechanical behaviour of 3D printed ultra-high performance concrete after elevated temperatures, Addit. Manuf. 58 (2022) 103032.
[32] W. Gao, Research on high-temperature resistance performance of hybrid-fiber reactive powder concrete, Western China Communications Science & Technology (2) (2016) 13–16.
[33] Y. He, H. Du, Residual compressive strength and ultrasonic testing after mixing fiber RPC at elevated temperature, Composites Science and Engineering (8) (2019) 78–81.
[34] B.A. Graybeal, Compressive behavior of ultra-high-performance fiber-reinforced concrete, ACI Mater. J. 104 (2) (2007) 146.
[35] T/CECS 10107-2020. Technical Requirements for Ultra High Performance Concrete.
[36] H. Wu, Y. Jiang, T. Pan, Y. Wang, Interlayer bonding property of a 3D printing cementitious material, New Building Materials 46 (12) (2019) 5–8.
[37] J.G. Sanjayan, B. Nematollahi, M. Xia, T. Marchment, Effect of surface moisture on inter-layer strength of 3D printed concrete, Construct. Build. Mater. 172 (2018) 468–475.
[38] B. Panda, S.C. Paul, N.A.N. Mohamed, Y.W.D. Tay, M.J. Tan, Measurement of tensile bond strength of 3D printed geopolymer mortar, Measurement 113 (2018) 108–116.
[39] C. Zhang, V.N. Nerella, A. Krishna, S. Wang, Y. Zhang, V. Mechtcherine, N. Banthia, Mix design concepts for 3D printable concrete: a review, Cement Concr. Compos. 122 (2021) 104155.
[40] GB/T 50081-2019. Standard for Test Methods of Concrete Physical and Mechanical Properties.
[41] GB/T 16777-2008. Test Methods for Building Waterproofing Coatings.
[42] International Organization for Standardization, ISO 834-1: 1999-Fire-Resistancetests-Elements of Building Construction-Part 1: General Requirements, 1999.
[43] X. Liu, Y. Yuan, G. Ye, G. De Schutter, Mechanism of polypropylene fibers on preventing spalling of self compacting concrete at high temperature, J. Tongji Univ. Nat. Sci. (7) (2007) 959–964.
[44] D. Gao, H. Li, F. Yang, Performance of polypropylene-steel hybrid fiber reinforced concrete after being exposed to high temperature, Fuhe Cailiao Xuebao 30 (1) (2013) 187–193.
[45] T. Yang, Z. Liu, Y. Yang, C. Wu, Experimental investigation on behavior of ultra-high performance concrete after high temperature, J. Civ. Environ. Eng. 42 (3) (2020) 115–126.
[46] Z. Mao, J. Zhang, Z. Luo, Q. Ma, Y. Duan, S. Li, Y. Miao, Behavior evaluation of hybrid fibre-reinforced reactive powder concrete after elevated temperatures, Construct. Build. Mater. 306 (2021) 124917.
[47] G. Li, Study on mechanical properties of reactive powder concrete with polypropylene fiber after high temperatures, New Building Materials 45 (6) (2018) 29–32.
[48] L. Sarvaranta, E. Mikkola, Fibre mortar composites under fire conditions: effects of ageing and moisture content of specimens, Mater. Struct. 27 (1994) 532–538.
[49] B. Panda, N.A. Noor Mohamed, S.C. Paul, G.V.P. Bhagath Singh, M.J. Tan, B. Šavija, The effect of material fresh properties and process parameters on buildability and interlayer adhesion of 3D printed concrete, Materials 12 (13) (2019) 2149.
[50] C. Yuan, J. Zhao, Damage mechanism of polypropylene fiber reinforced concrete exposed to high temperature, J. Mater. Sci. Eng. 35 (1) (2017) 37–40.
[51] P. Richard, M. Cheyrezy, Composition of reactive powder concretes, Cement Concr. Res. 25 (7) (1995) 1501–1511.
[52] L. Wang, Y. Chi, L. Xu, S. Liu, C. Yin, Size effect of mechanical properties of hybrid fiber ultra-high performance concrete, J. Build. Mater. 25 (8) (2022) 781–788.
[53] Y. Li, K.H. Tan, E.H. Yang, Synergistic effects of hybrid polypropylene and steel fibers on explosive spalling prevention of ultra-high performance concrete at elevated temperature, Cement Concr. Compos. 96 (2019) 174–181.
[54] Q. Yang, Study on high-temperature phase change of tobermorite, Spectrosc. Spectr. Anal. 33 (8) (2013) 2227–2230.
[55] Q. Zhao, Z. Wang, X. Xu, C. Cui, S. Zhang, X. Ding, Research status of structures, thermal behavior and synthesis of tobermorite, J. Chin. Ceram. Soc. 48 (10) (2020) 1536–1551.
[56] Z. Tian, L. Wang, X. Zhang, Formation mechanism and improvement solutions for weak interlayer surfaces of 3D printing concrete, Bulletin of the Chinese Ceramic Society 39 (7) (2020) 2052–2058.
[57] H. Li, Experimental Study on Spalling Behaviour and Mechanical Properties of Reactive Powder Concrete after Elevated Temperatures, Harbin Institute of Technology, 2012.
[58] J. Gao, J. Huo, s, in: The Reason of the Bond Face Being the Weakness of the Stressing Concrete of the Existing and Green Concrete, and Exploration of the Strengthening Measure, vol. 2, Journal of Jilin Jianzhu University, 2000, pp. 16–20.
[59] J.G. Sanjayan, B. Nematollahi, M. Xia, T. Marchment, Effect of surface moisture on inter-layer strength of 3D printed concrete, Construct. Build. Mater. 172 (2018) 468–475.
[60] S.C. Paul, Y.W.D. Tay, B. Panda, M.J. Tan, Fresh and hardened properties of 3D printable cementitious materials for building and construction, Arch. Civ. Mech. Eng. 18 (2018) 311–319.
[61] J. Zhao, J.J. Zheng, G.F. Peng, K. van Breugel, A meso-level investigation into the explosive spalling mechanism of high-performance concrete under fire exposure, Cement Concr. Res. 65 (2014) 64–75.
[62] L. Pham, P. Tran, J. Sanjayan, Steel fibres reinforced 3D printed concrete: influence of fibre sizes on mechanical performance, Construct. Build. Mater. 250 (2020) 118785.

[63] T.T. Le, S.A. Austin, S. Lim, R.A. Buswell, R. Law, A.G. Gibb, T. Thorpe, Hardened properties of high-performance printing concrete, Cement Concr. Res. 42 (3) (2012) 558–566.
[64] H. Zhang, L. Bai, Y. Qi, H. Hong, Q. Pan, Impact of splitting tensile properties and dynamic constitutive model of fly ash concrete, J. Mater. Civ. Eng. 32 (8) (2020) 04020225.
[65] Chinese National Standard, Code for Design of Concrete Structures, GB, 2010, pp. 50010–52010.